Granular Matter (2019) 21:48
https://doi.org/10.1007/s10035-019-0904-8

ORIGINAL PAPER

Micromechanical study of particle breakage in 2D angular rockfill media using combined DEM and XFEM

Javad Raisianzadeh[1] · Soheil Mohammadi[1] · Ali Asghar Mirghasemi[1]

Received: 1 November 2018

Abstract
A micromechanical study of particle breakage in 2D angular rockfill materials under biaxial compression loading has been conducted using a combined DEM and XFEM approach. In this approach, modeling of the crack propagation is performed on a fixed mesh without the limitations of classic FEM. Each breakage analysis is based on the final crack propagation state in the previous step; therefore, the progressive strength reduction of the particle is incorporated into the breakage analysis during loading. The micromechanics of the non-breakable and breakable assemblies have been studied under different confining pressures. It was found that particle breakage reduced the voids in the assembly, which resulted in a decrease in the final displacement of the particle assembly. Also, the contact forces, particle stresses and anisotropies decreased as a result of particle breakage and a more uniform distribution of contact forces and stresses was created. It was observed, as the confining pressure increased, the particle breakage increased and its effects intensified. Particle breakage was found to be the main cause of the decrease in anisotropies at higher confining pressures which, consequently, led to a reduction in the friction angle of the assembly.

Keywords Particle breakage · Micromechanics · Discrete element method · Extended finite element method · Macroscopic behavior

1 Introduction

Particle breakage in granular materials can occur at any stress level, but is primarily observed in soil-rockfill masses under high stress levels such as earthen dams and the subbases of railroad tracks. Particle breakage has been investigated in several experimental studies [1–8]. It is found that particle breakage significantly affects the behavior of granular materials, including the shear strength and compressibility.

The discrete element method (DEM) aids in the investigation of various aspects of the macroscopic behavior of granular materials. Detailed study of the microstructure of granular materials is hardly possible through experimental tests, but can be performed using DEM.

In a particle assembly, external loads applied to the boundary particles are distributed in the assembly through contact between particles. The size, geometry, material type and arrangement of the particles within the assembly affect the distribution of contact forces. These factors, as well as the type of loading applied to the particle assembly, are involved in the formation of anisotropy in the assembly. Anisotropy affects the shear strength and macroscopic behavior of the particle assembly; therefore, it is necessary to study the microstructure of a particle assembly in order to better understand its macroscopic behavior.

Various DEM-based numerical models have been used to study particle breakage in granular materials [9–32]. In one series of models [18, 19], each breakable particle was simulated as an agglomerate of bonded unbreakable spheres or disks in a crystallographic array. In this case, breakage occurred when the contact forces between the spheres or disks exceeded a defined value. Such models frequently have been used for simulation of particle breakage in sand [20–24], but reproducing angular particles, such as rockfill, using an agglomerate of spheres or disks is of limited accuracy or requires a large number of particles at high computational costs. Hosseininia and Mirghasemi [25, 26] modeled breakage of 2D angular particles by replacing each particle

✉ Ali Asghar Mirghasemi
aghasemi@ut.ac.ir

[1] School of Civil Engineering, College of Engineering, University of Tehran, Tehran, Iran

Published online: 03 June 2019

with bonded polygonal sub-particles. In their model, as in previous models, failure of the bonds between the sub-particles simulated the breakage.

In another approach, a combined finite-discrete element method was used for breakage simulation of angular particles by Bagherzadeh-Khalkhali et al. [27, 28]. In their study, first the interaction between particles was modeled by DEM, then each particle was meshed individually and a stress–strain analysis was performed using finite element method (FEM). Breakage was modeled based on the number of plastic elements in the particle along a best fit line through these elements. Luo et al. [29] updated this approach by modeling each particle with a single polygonal element using scaled boundary finite element method (SBFEM), instead of discretizing each particle into a large number of elements. Ma et al. [30–32] used a finite-discrete element approach to model breakage of 2D and 3D particles. In their approach, cohesive interface elements were inserted at the boundaries between elements according to the cohesive crack model. Breakage was simulated by failure of the interface elements along the boundary between the elements.

In the models described above, simplifying assumptions were used for breakage simulation. These models required extensive calibration with experimental data to produce reasonable results. Furthermore, the crack propagation history, which affects the potential breakage of the particle, was not incorporated. In fact, the propagation of a crack in the particle may result in breakage or a stop at some point, but these models did not simulate the progressive propagation of the crack and breakage occurred instantaneously.

The current study aimed at removing these shortcomings in breakage modeling by combining the DEM and extended finite element method (XFEM). Biaxial compression testing on a 2D granular assembly of angular rockfill particles has been simulated and the micromechanical behavior investigated. It should be noted that a corresponding macroscopic study has been presented [33].

2 Breakage modeling

Figure 1 shows flowchart of algorithm used for simulation of breakage of angular particles in the present study. In the proposed approach, simulation of the particle assembly under biaxial compression loading is performed using the DEM. During loading and at short time intervals, breakage analysis is performed separately on each particle using XFEM. At this stage, each particle is analyzed for crack initiation or propagation under contact loads from adjacent particles. If the crack propagation results in breakage, the initial particle is divided into two separate particles along the final breakage path.

The DEM simulation of assembly of angular particles was performed by modifying the POLY program which was previously introduced by Mirghasemi et al. [34, 35]. In addition, a new code was developed for the XFEM breakage analysis of particles. These two programs were combined to simulate the particle breakage under biaxial testing. The DEM and breakage analysis are briefly reviewed in Sects. 2.1 and 2.2, respectively. The numerical model is briefly described in this section. Full details of the model have been presented in [33].

2.1 Simulation of particle assembly by DEM

As noted, simulation of the particle assembly under biaxial loading is performed using DEM. The contact forces applied to each particle are used as the inputs for the XFEM breakage analysis of the particle. Flowchart of each calculation cycle in DEM is shown in Fig. 2. As seen, after applying the boundary conditions to the assembly, contacts between particles are detected by using the position of the particles at the beginning of the time step. The contact forces then are calculated using a contact constitutive model. Deformation of each particle is negligible in comparison with the particle assembly deformation; therefore, each particle could be assumed to be rigid. As a result, the contact forces are determined by calculating the area of overlap between two particles.

The resultant force applied to each particle is obtained by calculating all contact forces from adjacent particles. The acceleration of each particle can be calculated using Newton's second law and the resultant force acting upon the particle. In an approach similar to that of the finite difference method, the new velocity of the particle is determined by integration of its acceleration over the current time step. Integration of the velocity yields the new position of the particle at the end of the time step. The new velocity, position of the particles and inter-particle forces at the end of the current time step are considered to be the initial conditions for the next cycle of calculations. These stages are used to construct each cycle of calculation in DEM simulation.

Because dynamic equilibrium equations are used in each calculation cycle of DEM simulation, the out-of-balance forces should be very small to simulate a particle assembly under static equilibrium. In order to approach static equilibrium, a very small time step is used in DEM simulation. If the time step is small enough, displacement of each particle within that time step will be small. Therefore, the particle only will affect the adjacent particles during each time step and the movements will not propagate further in the assembly, which eventually results in static equilibrium [36]. The velocity and acceleration of the particles can be assumed to be constant during each time step under this condition.

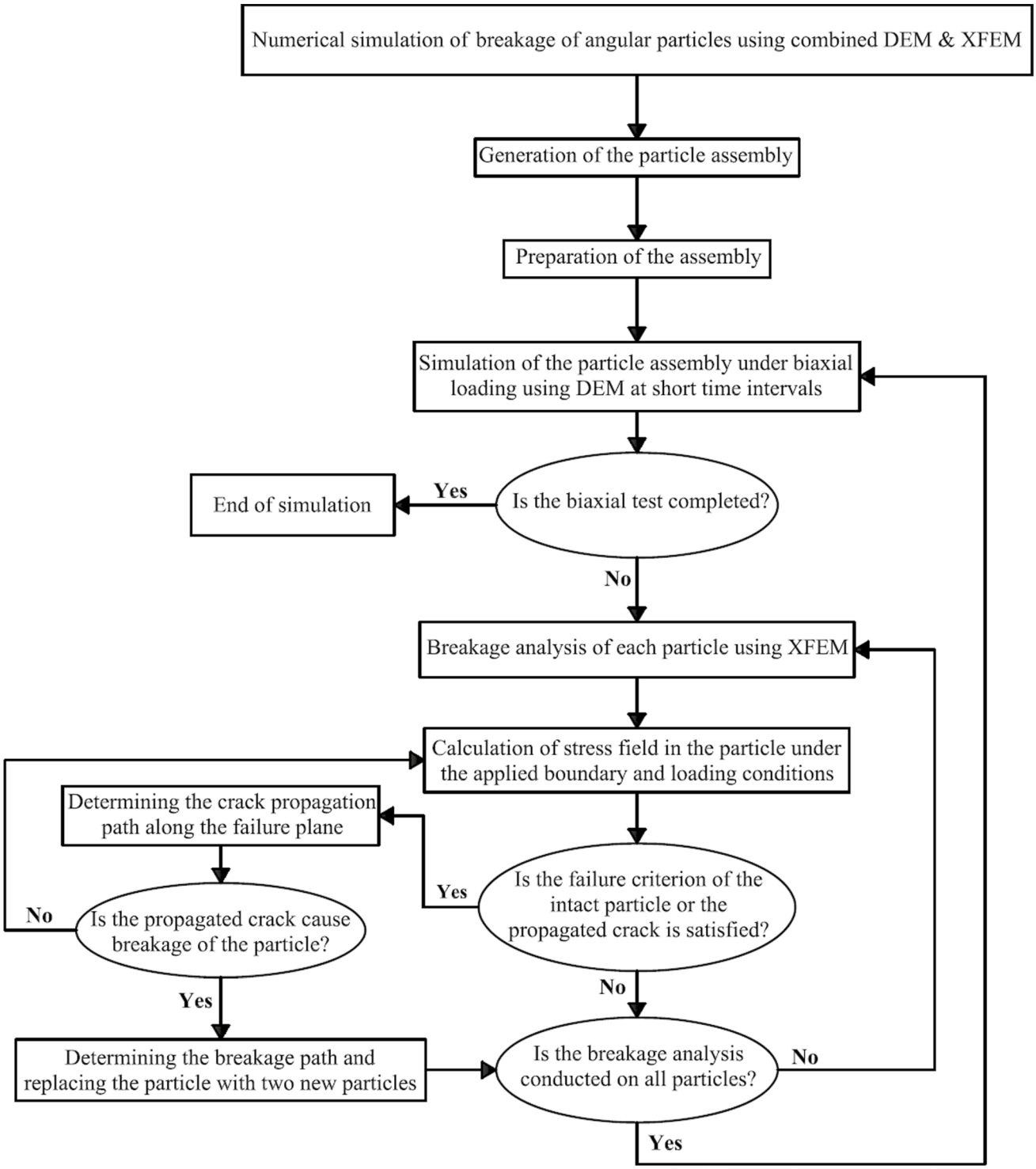

Fig. 1 Flowchart of algorithm used for simulation of breakage of angular particles

In this study, the angular rockfill particles are modeled as convex polygons. There are a limited number of polygonal shapes in the assembly, which creates different types of particles. The particle assembly is randomly generated in a circular area based on the initial number of particles and the particle size distribution. These factors determine the number of each particle type in the assembly.

Loading is applied to the particle assembly under both stress-controlled and strain-controlled conditions by applying a sufficient velocity to the boundary particles. In fact,

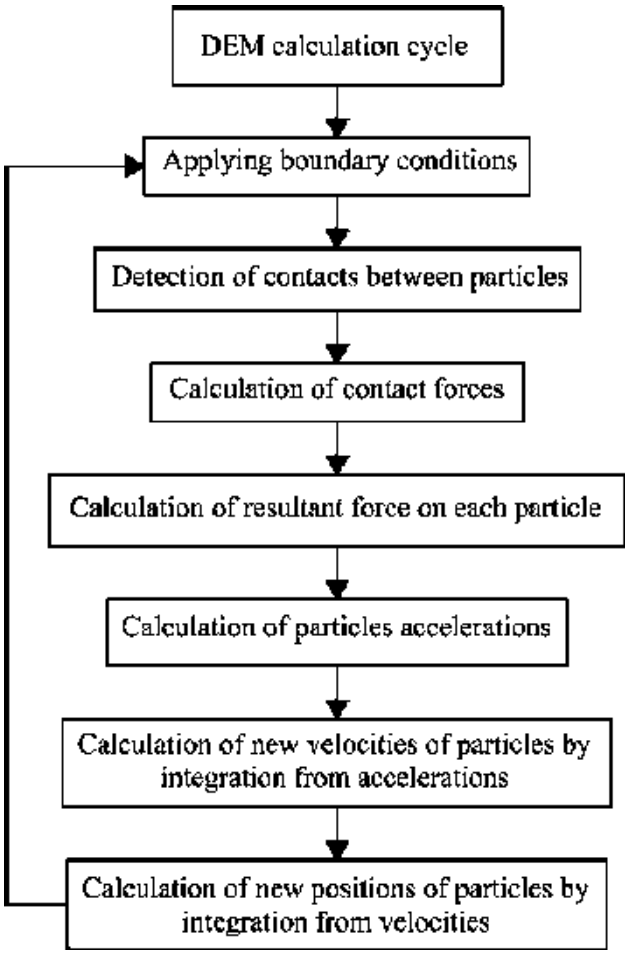

Fig. 2 Flowchart of each cycle of DEM calculation

moving the boundary particles at certain velocities creates the desired stress or strain in the assembly. Because of the essential role of the boundary particles in applying a load to the assembly, breakage of these particles is not allowed during loading.

2.2 Particle breakage analysis using XFEM

Each particle of the assembly is assumed to be intact at the beginning of biaxial test. Breakage analysis is repeated on all particles during biaxial loading. Each particle is meshed separately and then XFEM stress–strain analysis is performed on the particle. The loads applied on the particle are the contact forces from adjacent particles and are calculated using the DEM analysis in the intended time step. If the particle has at least three contacts with adjacent particles, two contact points are considered to be fixed points in a way that it would not cause instability and constitute a statically determinate system. The contact forces of the other contact points are applied as external loads on the particle.

The stress field in the intact or cracked particles could be obtained using XFEM. XFEM is based on classic FEM but does not have the limitations of FEM concerning the modeling of crack propagation problems. In classic FEM, the crack cannot pass through an element of the mesh and should propagate along the boundaries of the elements [37, 38]. For general non-conforming crack propagations, a remeshing scheme should be used which, however, increases the computational costs [37, 38]. In the XFEM model used in the present study, crack propagation is modeled on a fixed mesh and in different time steps by adding an enrichment function to the standard FEM approximation. This model eliminates the limitations of crack propagation as encountered in classic FEM.

In the XFEM model used in this study, an enrichment function is added to the conventional FEM approximation of the unknown displacement u to model the discontinuity as:

$$u^h(x) = \sum_{\forall I} N_I(x)u_I + \sum_{J\in S_H} N_J(x)\left[H(f(x)) - H\left(f\left(x_J\right)\right)\right]q_J \tag{1}$$

where x is an arbitrary point in the domain of the problem. In the right side of Eq. (1), the first term is the conventional FEM solution where N represents the shape functions and u_I is the conventional degrees of freedom. The second term enables modeling of the discontinuity using the Heaviside enrichment functions. S_H represents the nodes located adjacent to the crack. Additional degrees of freedom q_J having the same number and direction as the conventional degrees of freedom are added at every node of S_H [37, 38]. In fact, in the S_H domain of a 2D model, two additional horizontal and vertical degrees of freedom are assigned to every free node. The addition of $H\left(f\left(x_J\right)\right)$ to the enrichment term in Eq. (1) satisfies the interpolation at all nodes. In this case, u is equal to the real displacement on all nodes, including enriched node k [37, 38]:

$$u^h\left(x_k\right) = u_k + \left[H\left(f\left(x_k\right)\right) - H\left(f\left(x_k\right)\right)\right]q_k = u_k \tag{2}$$

One of the frequently used Heaviside enrichment functions is the sign function:

$$H(\xi) = sign(\xi) = \begin{cases} +1 & \forall \xi > 0 \\ -1 & \forall \xi < 0 \end{cases} \tag{3}$$

where ξ is the signed distance from the considered point to the adjacent crack. Therefore, in Eq. (1), $f(x)$ and $f\left(x_J\right)$ would be the signed distances from arbitrary point x and enriched node J to the adjacent crack, respectively. The displacement discontinuity between the two sides of the crack can be modeled using this function. In XFEM crack modeling, limitations of crack propagation on a conventional fixed mesh are removed. In the present study, the crack is allowed to propagate in only one element at each step of breakage analysis. Propagation of the crack to a boundary

of the particle is assumed to be equivalent to the breakage of that particle.

The rockfill materials considered show brittle behavior under compressive loads; thus, linear elastic material behavior is used in the breakage analysis. Further detail about the XFEM numerical modeling is available in [33].

The Hoek–Brown failure criterion is used as a criterion for crack propagation in the particle and to determine the angle of the crack propagation path. This criterion is widely used in determining the failure of various types of rock [39]:

$$\sigma_{1f} = \sigma_{3f} + \sigma_{ci}\left(m_i \frac{\sigma_{3f}}{\sigma_{ci}} + 1\right)^{0.5} \tag{4}$$

where σ_{1f} and σ_{3f} are the major and minor principal stresses, respectively, σ_{ci} is the uniaxial compressive strength of the rock and m_i is a constant coefficient which is determined based on the type of rock and its properties [39]. According to this criterion, if the major principal stress is greater than or equal to σ_{1f}, shear failure occurs. According to Eq. (4), the tensile strength is $\sigma_t = \frac{-\sigma_{ci}}{m_i}$ and, if the tensile stress is greater than or equal to this value, tensile failure occurs. Failure of the elements of a particle can be determined using the following safety factors:

$$SF_i = \frac{\sigma_{1f}}{\sigma_{1i}};\ \text{Shear failure} \tag{5}$$

$$SF_i = \frac{\sigma_t}{\sigma_{3i}};\ \text{Tensile failure} \tag{6}$$

where σ_{1i} and σ_{3i} are the major and minor principal stresses in element i, respectively. These stresses are determined based on the stress field obtained from the XFEM stress–strain analysis of the particle. If the safety factor of an element from Eqs. (5) or (6) is smaller than 1, failure occurs in either shear or tensile mode, respectively.

According to the Hoek–Brown criterion, the failure plane of the shear mode has an angle of $\beta = \pi/4 + \varphi/2$ with respect to the major principal stress direction. If failure occurs in the tensile mode, the failure plane will be perpendicular to the tensile stress direction.

For intact particles, the first element that reaches a safety factor of less than 1 is assumed to be the crack initiation point. The crack angle is determined along the direction of the shear or tensile failure plane in the Hoek–Brown criterion. The XFEM stress–strain analysis then is repeated on the cracked particle and the stress field in the particle is updated. Based on the updated stress field, if the safety factor of the elements adjacent to the crack tip is less than 1, the crack propagates along the shear or tensile failure plane in only one element. These steps are repeated upon further propagation of the crack and continue until the crack propagation results in particle breakage or the crack stops in the particle. As soon as the crack reaches a boundary of the particle, breakage occurs and the breakage path is determined as a straight line connecting the initial and final points of the crack propagation path. The particle is divided into two new separate particles along the breakage path. The new particles are assumed to be at the position of the initial particle in the assembly with properties similar to those of the initial particle.

When the XFEM breakage analysis has been performed on all particles, the biaxial loading on the particle assembly continues. In the DEM analysis, all particles, including the new ones, are subjected to contact loads. In the next series of the XFEM breakage analysis, the new particles are meshed and analyzed similarly to the other particles; therefore, further breakage of the new particles is possible. The XFEM breakage analysis is repeated on all particles at small time intervals until the end of the biaxial test.

In the proposed model, the usual simplifying assumptions for determining the breakage path have been removed. Modeling of crack propagation can be performed on a fixed mesh without the limitations of classic FEM. In this model, the crack propagates step-by-step based on the boundary and loading conditions of the particle. In each step, the stress–strain analysis is performed based on the crack propagated in the previous steps. In this way, progressive strength reduction of the particle can be effectively simulated in the breakage analysis.

A series of conventional laboratory tests have been simulated on intact rock specimens to investigate the ability of the proposed breakage model. The results of these simulations, which have been presented by Raisianzadeh et al. [33], showed ability of the model to predict the breakage path and breakage strength under different boundary and loading conditions.

3 Simulation of biaxial tests

The effects of particle breakage on the behavior of the particle assembly were investigated by simulation of compression biaxial tests in two groups of non-breakable and breakable particles. In the first group, the breakage of particles was disabled and, in the second group, the breakage of particles was enabled. The biaxial tests were performed under drained conditions on an assembly of 1194 angular rockfill particles. The particles of the assembly have diameters of 37 to 57 cm and are uniformly distributed throughout this range. The particles were meshed on the basis of size and number of edges to produce the accuracy required for the breakage analysis. Each particle was meshed using 75 nodes and 120 elements on average, which resulted in about 79,500 nodes and 130,700 elements for each XFEM analysis. It is evident

that the number of nodes and elements used in each XFEM analysis increased as particle breakage occurred during the biaxial test.

As noted in Sect. 2.1, the assembly used in the biaxial test was generated randomly in a circular area. This particle assembly was very loose; thus, a strain-controlled load was applied in the next stage to compact the assembly. Compaction continued until the particles were in slight contact with each other, then it was relaxed. At this stage, slight movement of particles in their positions reduced the contact between particles to a minimum. Next, a stress-controlled load was applied to the assembly to establish the determined confining pressure for biaxial testing. Application of the load continued until the average horizontal stress of the particle assembly became constant and equal to the determined confining pressure in which the volume (area in two dimensions) of the particle assembly reached a constant value. The biaxial tests were performed under confining pressures of 0.5, 1, 2 and 4 MPa. In order to compare test results under similar conditions, all specimens were prepared such that the void ratio had the same value of $e = 0.3$ before biaxial loading.

The biaxial test was initiated by applying a vertical compressive load with a constant strain rate while the stress of the assembly in the horizontal direction was kept constant and equal to the confining pressure. A very small strain rate was used for loading to ensure quasi-static conditions during the test. Shear loading continued up to a strain of 16–18% in the different biaxial tests.

The values of the parameters used for the DEM and XFEM breakage analyses are presented in Table 1. These values were selected empirically because of the qualitative nature of this research.

4 Results and discussion

4.1 Microstructure of particle assembly

Figure 3 shows the contour of particles displacement during biaxial testing at a confining pressure of 2 MPa for the non-breakable and breakable assemblies. New particles created by breakage are shown in black. As seen, particles in the central area show slight displacement in both groups, while the particles in outer area show greater displacement. Because of the greater displacement gradients in the outer areas, particle breakage occurred more in these areas than in the central area. The movement of the new particles created by breakage into the voids between the existing particles reduced the total void ratio in the assembly (see Table 4). Comparison of the displacement contours of the non-breakable and breakable assemblies shows a decrease in maximum displacement in the breakable assembly due to breakage and production of new particles. This difference is more evident at the end of the biaxial test, where a significant percentage of particle breakage could be observed. In fact, the decrease in voids reduced the dilative behavior of the assembly and the final displacement of particles.

Figure 4 shows the normal contact force chains during biaxial testing at a confining pressure of 2 MPa for the non-breakable and breakable assemblies. The contact forces are shown at three levels: weak, moderate and strong. The distribution of the vertical and horizontal particle stresses are shown for both groups in Figs. 5 and 6, respectively. As for the force chains, the stresses are shown as being low, medium or high. The stresses of each particle were calculated by averaging the finite elements stresses obtained from the XFEM analysis during the biaxial test. As seen in Fig. 4, at the beginning of the test, the contact force chains were mainly consisted of uniform weak forces. Moderate and strong force chains gradually increased in a non-uniform distribution as shear loading increased. These force chains were mainly formed vertically, but the magnitude of the horizontal contact forces remained relatively small. This trend can be observed in Figs. 5 and 6 as well. The moderate and high vertical stresses increased during biaxial loading, but the horizontal stresses increased slightly at the beginning of the test and then remained relatively constant. This indicates that the difference between vertical and horizontal stresses increased as the shear loading increased.

As seen in Figs. 4, 5 and 6, the moderate and strong contact forces induced medium and high vertical stresses in particles along the vertical chains in the assembly. The vertical stress level decreased in particles as the loading increased past an axial strain of about 10% due to the failure of the vertical force chains, especially the strong force chains. In fact, the highest level of contact forces and stresses occurred at an axial strain of 10% which created the peak shear strength of the particle assembly.

Comparison of force chains for the non-breakable and breakable assemblies shows that the contact forces were distributed more uniformly and strong forces decreased because of particle breakage. This was more evident at high strains where a higher percentage of particle breakage was

Table 1 Parameters used in the DEM–XFEM model for simulation of biaxial testing

Parameter	Value
Density of particles (kg/m^3)	2500
Inter-particle friction coefficient	0.5
Normal and tangential stiffness (N/m)	2×10^7
Uniaxial compressive strength (MPa)	150
Hoek–Brown parameter, m_i	25
Elastic modulus (GPa)	20
Poisson's ratio	0.2

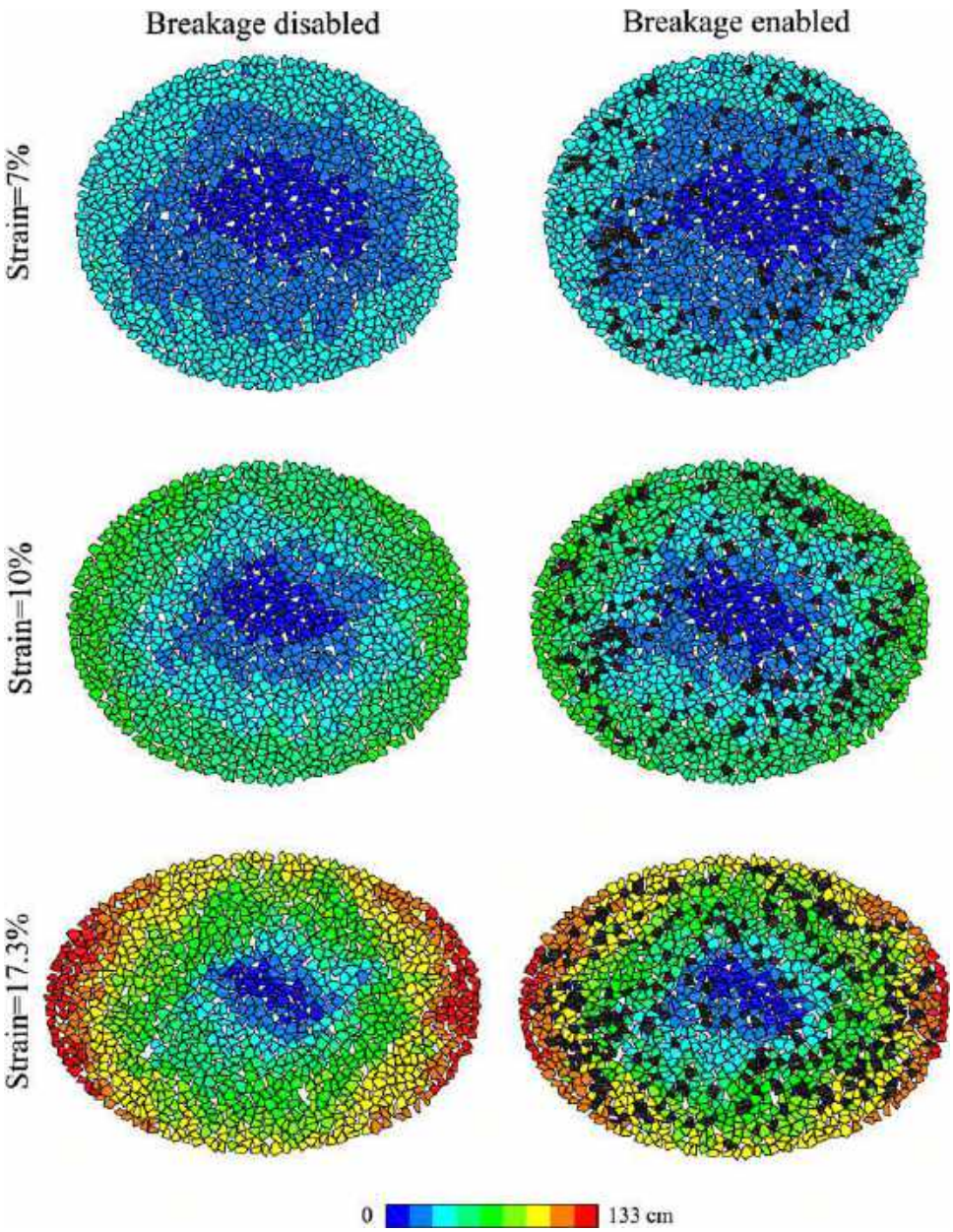

Fig. 3 Contour of particles displacement during biaxial testing at a confining pressure of 2 MPa for non-breakable and breakable assemblies

observed. In fact, when particles broke, the force chains failed before reaching their loading limit. Also, the magnitude of the forces decreased as new smaller particles created by breakage increased because the contact forces produced between the smaller particles were lower [40]. The decrease in contact forces caused a more uniform distribution of forces in the assembly. The failure of the strong force chains and redistribution of contact forces removed the stress concentrations and reduced high stresses in the breakable assembly (Fig. 5).

In order to quantitatively demonstrate the differences between Figs. 3, 4, 5 and 6, the number of particles at different levels of displacement and stress and the number of forces at different levels were measured in each figure and are shown in Table 2. The collected data confirms the observations mentioned previously. As observed in Table 2, the number of strong forces and particles under high stresses increased during biaxial loading until peak shear strength was attained and then these numbers decreased slightly. Moreover, particle breakage reduced the number of strong forces and particles under high stresses. It also can be seen that the number of particles experiencing large displacements (> 118 cm) in the breakable assembly decreased compared to that in the non-breakable assembly. In other words, displacement of the particle assembly decreased due to particle breakage.

Figure 7 shows the probability density functions (PDFs) of normal contact forces at different levels of strain during

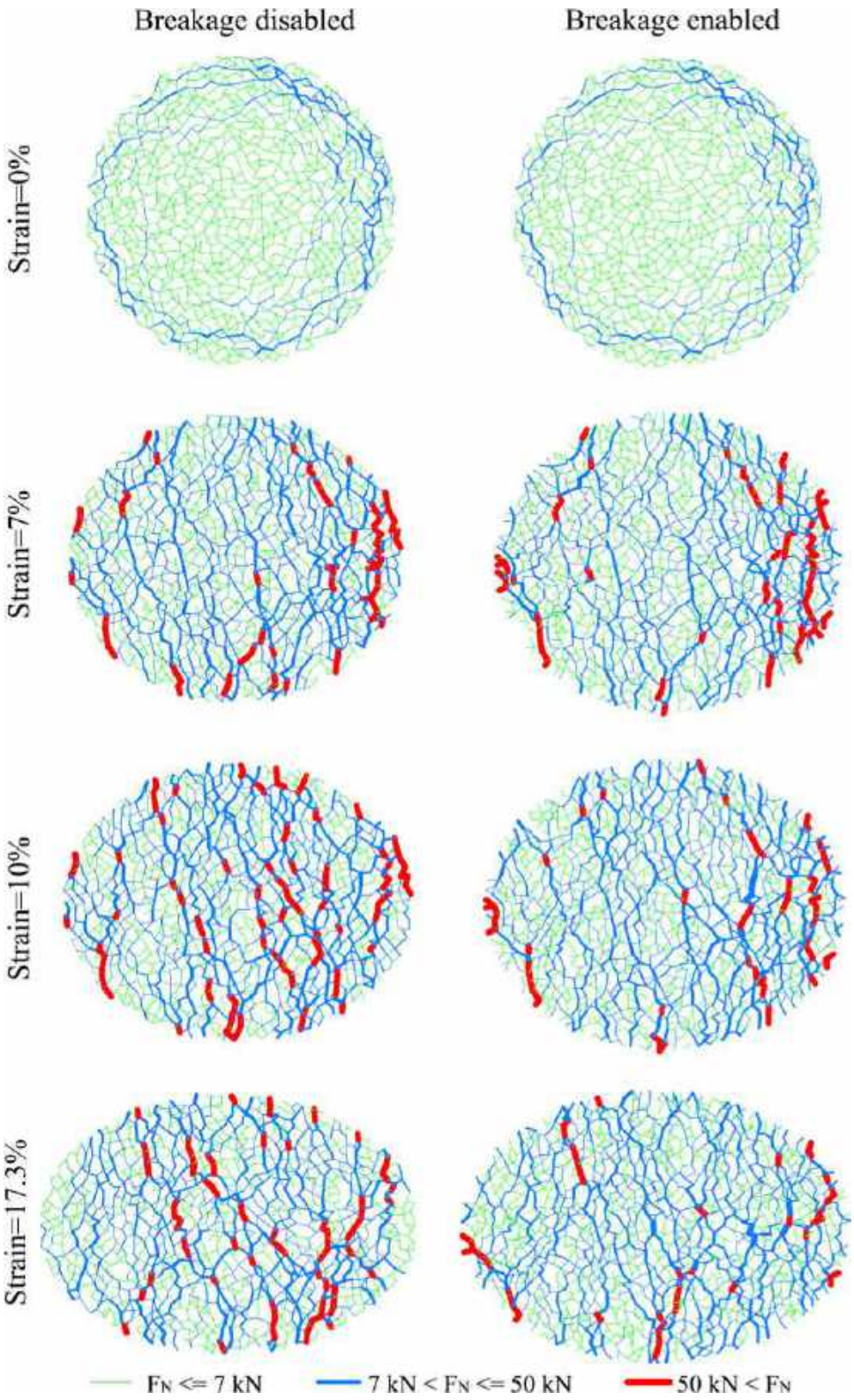

Fig. 4 Normal contact force chains during biaxial testing at a confining pressure of 2 MPa for non-breakable and breakable assemblies

biaxial loading under a confining pressure of 2 MPa. As seen, a larger number of forces had low values at the beginning of the test and the number of strong forces decreased exponentially. The number of strong forces increased as the axial strain increased. Moreover, particle breakage increased the number of low-value forces and

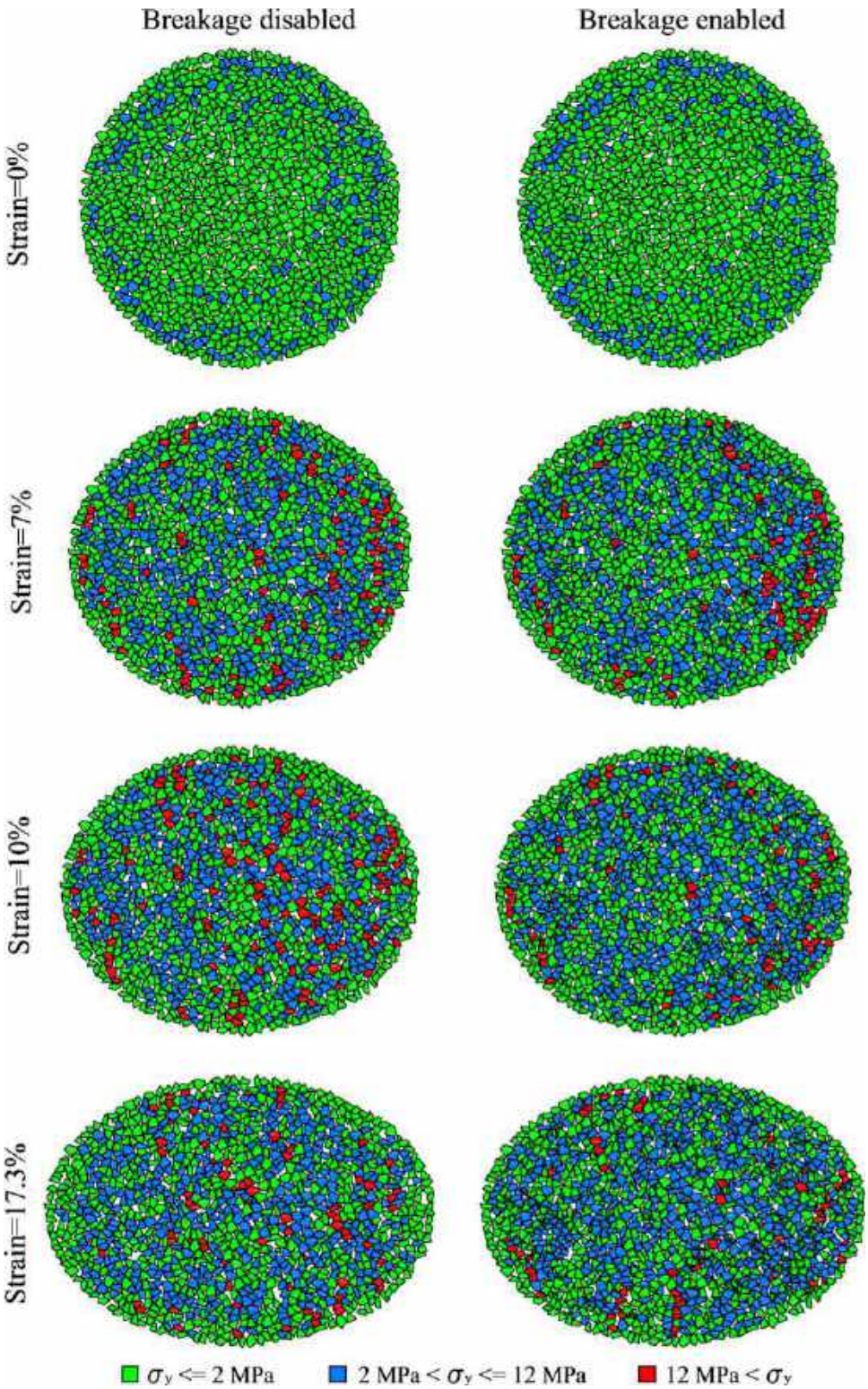

Fig. 5 Distribution of vertical particle stresses during biaxial testing at a confining pressure of 2 MPa for non-breakable and breakable assemblies

decreased the number of strong forces. In fact, a more uniform distribution of forces was created because of particle breakage. This also can be observed in Fig. 4.

4.2 Anisotropies

A series of directional distributions are used for the contact orientation and normal and shear contact forces in order to study the microstructure of a particle assembly and its

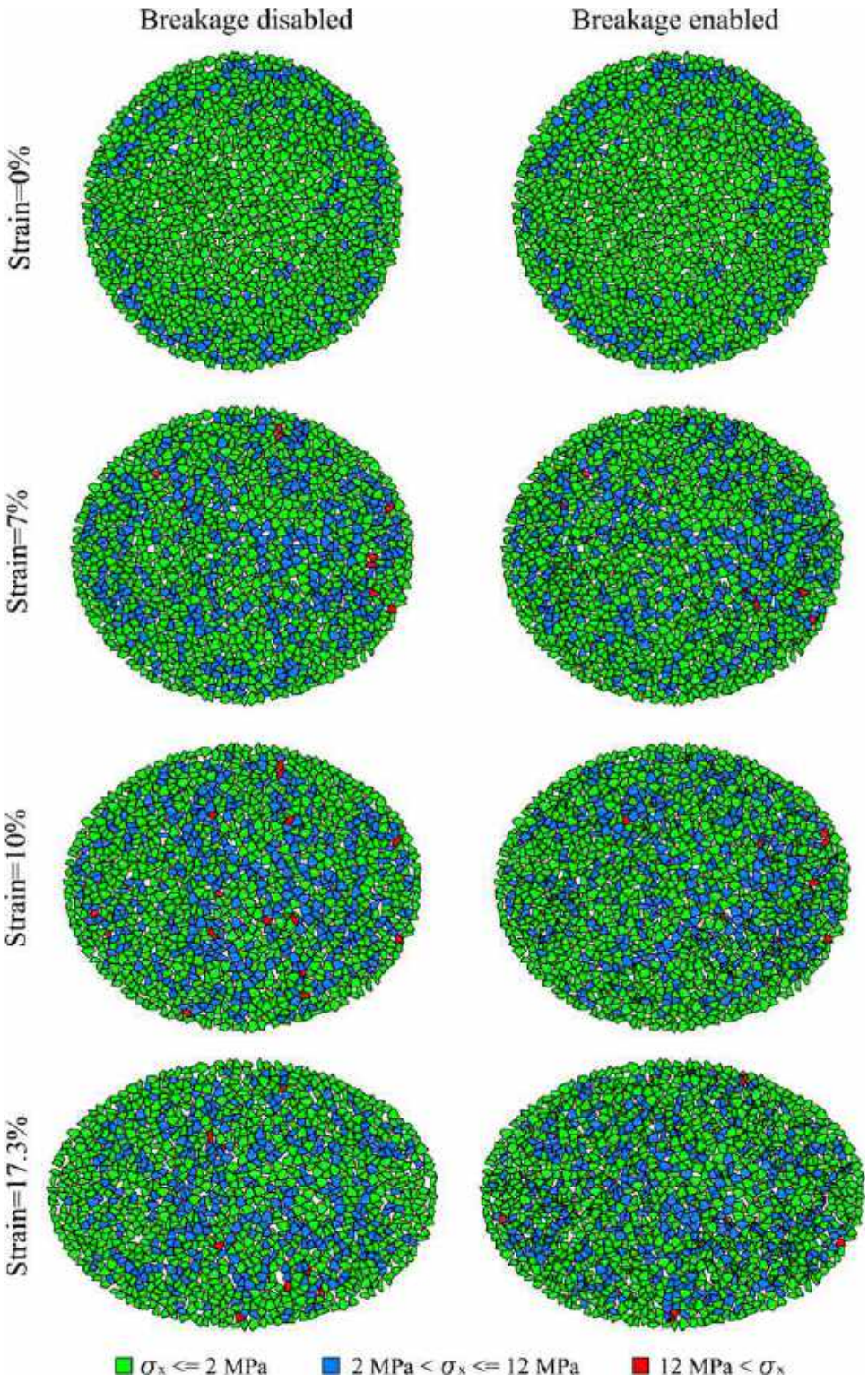

Fig. 6 Distribution of horizontal particle stresses during biaxial testing at a confining pressure of 2 MPa for non-breakable and breakable assemblies

effects on macroscopic behavior. Figure 8 shows that the unit vector of contact $\boldsymbol{n}$ is perpendicular to the direction of contact between two particles. The direction of this vector represents the direction of the contact. Distribution of contact orientation $E(\theta)$ in a particle assembly is defined as the total number of contacts having direction θ that fall within angle range $\left(\theta - \frac{d\theta}{2}, \theta + \frac{d\theta}{2}\right)$ for angle increment $d\theta$. This distribution is introduced as follows using the second-order Fourier expansion [45]:

Table 2 Number of particles having large displacements, and number of forces and stresses at different strain levels under a confining pressure of 2 MPa

Axial strain	Non-breakable assembly				Breakable assembly			
	0%	7%	10%	17.3%	0%	7%	10%	17.3%
Number of large displacements (> 118 cm) at the end of the test	0	0	0	86	0	0	0	41
Number of weak forces	1619	697	661	717	1619	963	938	1091
Number of moderate forces	396	1198	1165	1118	396	1215	1344	1372
Number of strong forces	0	92	121	85	0	78	56	40
Number of low vertical stresses	1005	610	586	616	1005	797	824	881
Number of medium vertical stresses	189	482	476	493	189	459	527	589
Number of high vertical stresses	0	102	132	85	0	88	60	43
Number of low horizontal stresses	1008	819	795	827	1008	994	1037	1114
Number of medium horizontal stresses	186	366	383	359	186	338	360	388
Number of high horizontal stresses	0	9	16	8	0	12	14	11

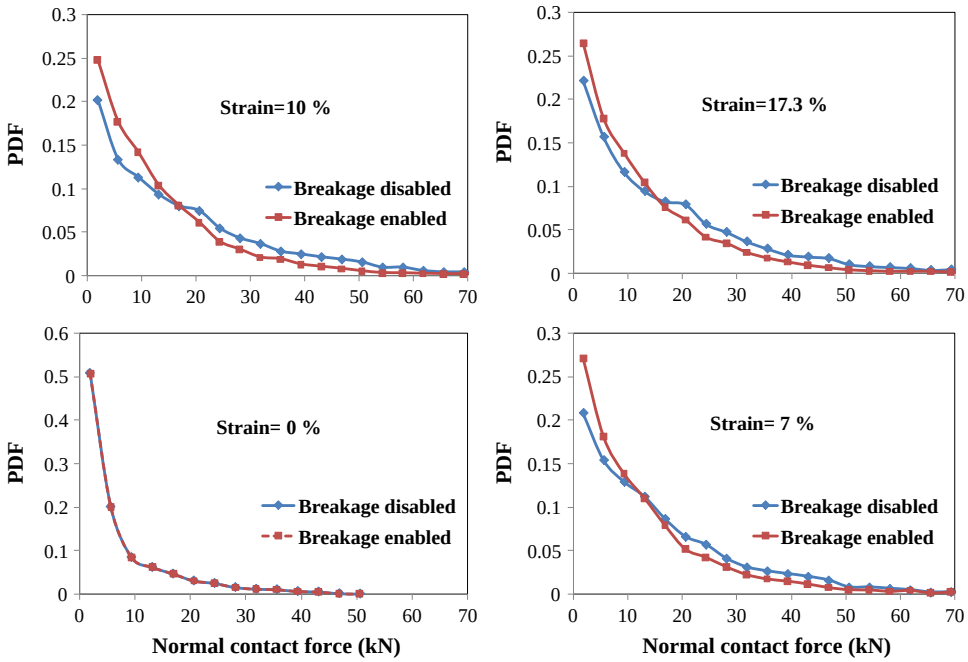

Fig. 7 PDFs of normal contact forces at different levels of strain during biaxial loading under a confining pressure of 2 MPa. To better illustrate the differences between non-breakable and breakable assemblies, the figures related to strain levels greater than zero are shown at smaller scale

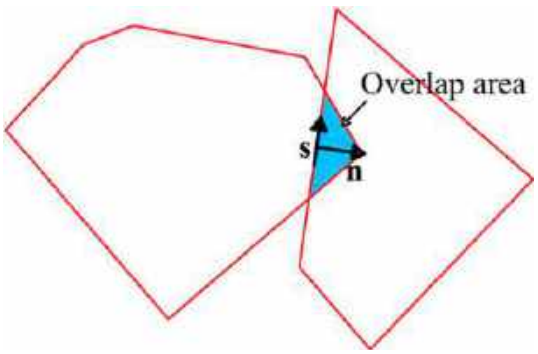

Fig. 8 Typical contact between two polygonal particles

$$E(\theta) = \frac{1}{2\pi}\left[1 + a\cos 2\left(\theta - \theta_0\right)\right] \tag{7}$$

where a is the anisotropy of contact orientation and θ_0 is the principal direction of anisotropy. According to Eq. (7), the number of contacts oriented along θ_0 is proportional to $1 + a$ and the number of contacts oriented perpendicular to θ_0 is proportional to $1 - a$. As a result, a is proportional to the difference in the number of contacts oriented along these two directions.

The contact force between two particles can be decomposed into the normal contact force component (along the vector $\boldsymbol{n}$) and shear contact force component (perpendicular to the vector $\boldsymbol{n}$), as shown in Fig. 8. Functions of the average normal forces $\overline{f}_n(\theta)$ and average shear forces $\overline{f}_s(\theta)$ are

determined as the average of the normal and shear forces of the contacts oriented along θ, respectively. These functions also can be expressed using the second-order Fourier expansion [45] as:

$$\overline{f}_n(\theta) = \overline{f}_0\left[1 + a_n \cos 2\left(\theta - \theta_n\right)\right] \tag{8}$$

$$\overline{f}_s(\theta) = \overline{f}_0\left[a_t \sin 2\left(\theta - \theta_t\right)\right] \tag{9}$$

where $\overline{f}_0$ is the average of all contact forces in a particle assembly, a_n and a_t are the anisotropies of the normal and shear contact forces, respectively, and θ_n and θ_t are the principal directions of the anisotropy of normal and shear forces, respectively. As in Eq. (7), a_n is proportional to the difference in the average normal forces of the contacts oriented along and perpendicular to the principal direction of the normal force anisotropy and a_t is proportional to the difference in the average shear forces of the contacts oriented along and perpendicular to the principal direction of the shear force anisotropy.

Figures 9, 10 and 11 show the polar distribution of the contact orientation and normal and shear contact forces, respectively, under a confining pressure of 2 MPa. The polar distribution of the non-breakable assembly has been compared to that of the breakable assembly at the beginning of biaxial testing, at peak shear strength and at the end of loading. Because an isotropic loading was applied to the assembly before biaxial loading, the histograms of the contact orientation and normal contact forces were almost circular at the beginning of the test, which indicates a rather uniform distribution of these parameters in different directions. Moreover, the inter-particle shear contact forces were approximately zero and the particles only applied normal contact forces to each other when isotropic loading was applied. It can be observed that the shear forces were very small and approached zero at the beginning of the test.

When biaxial loading was applied, a number of contacts were lost in the horizontal direction due to horizontal expansion of the specimen. On the other hand, as particles approached each other vertically and formed new contact chains, the number of contacts increased in the vertical

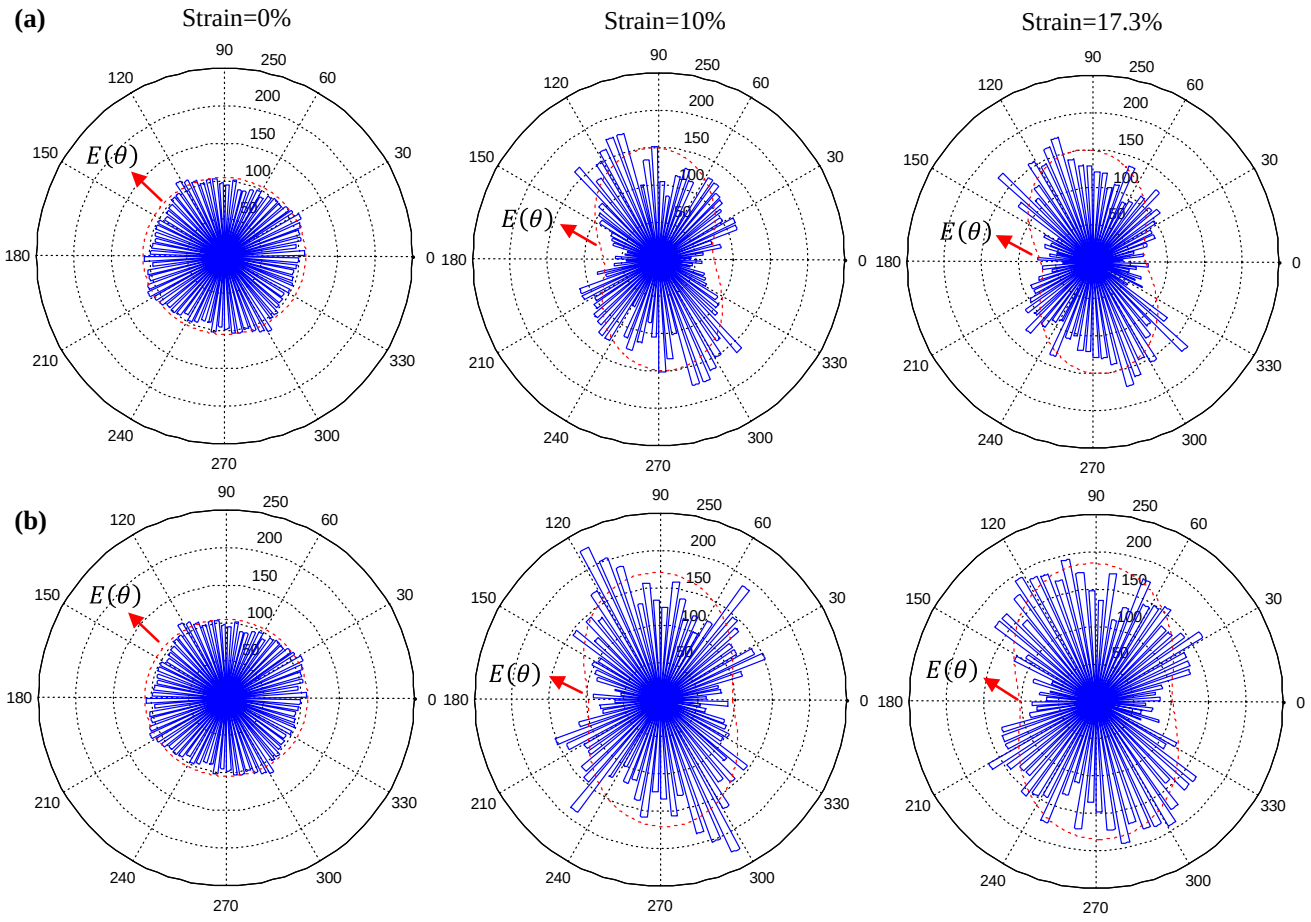

Fig. 9 Histogram of contact orientation at three strain levels during biaxial testing under a confining pressure of 2 MPa for: **a** non-breakable assembly; **b** breakable assembly

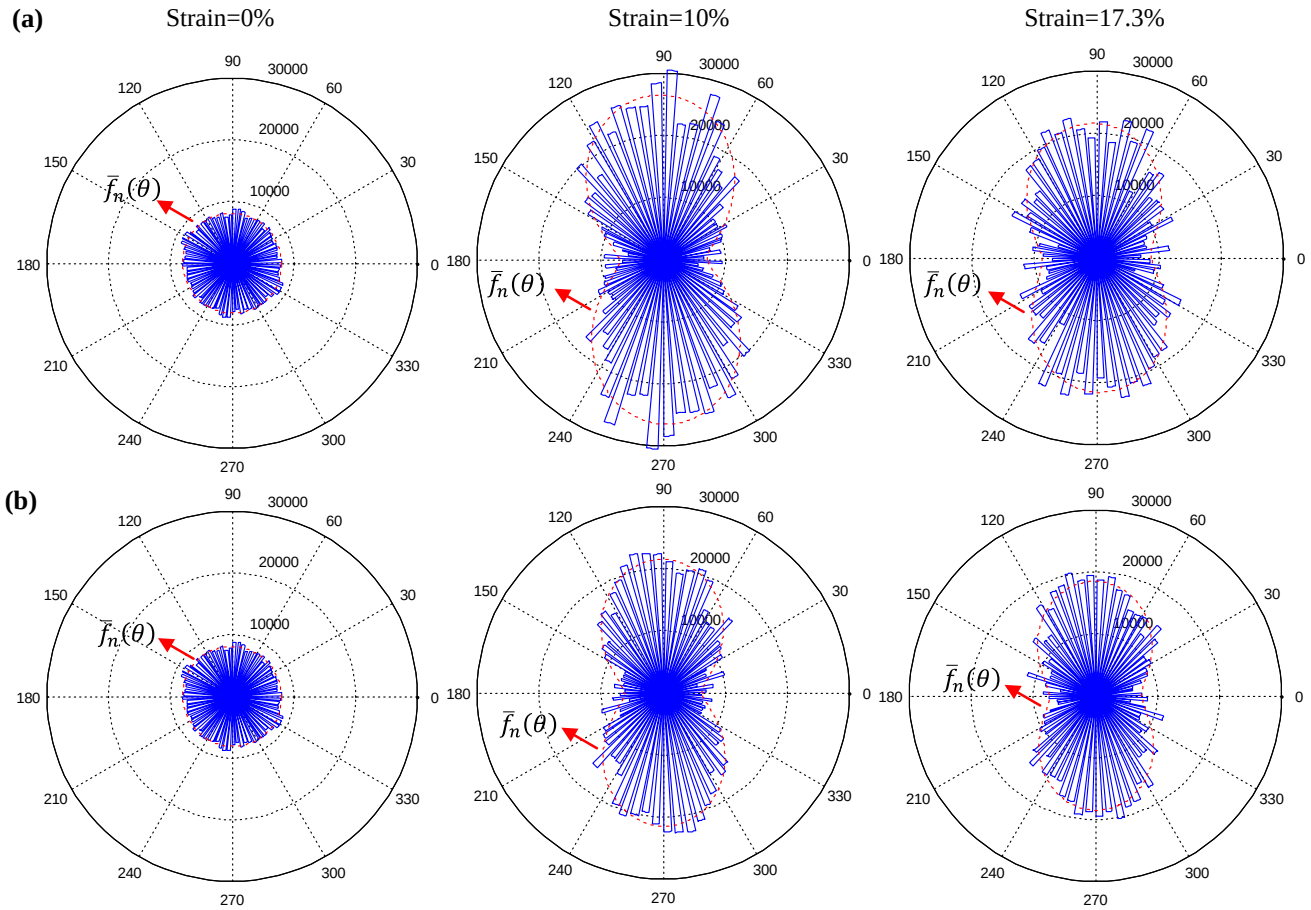

Fig. 10 Histogram of normal contact forces at three strain levels during biaxial testing under a confining pressure of 2 MPa for: **a** non-breakable assembly; **b** breakable assembly

direction. Consequently, as observed in Fig. 9, the difference in the number of vertical and horizontal contacts increased during biaxial testing, which indicates an increase in the anisotropy of the contact orientation. This is evidenced by the histograms forming a peanut shape at the end of the test. Comparison of the histograms for the non-breakable and breakable particles shows that new contacts formed due to particle breakage and generation of new particles. The increase in the number of contacts occurred in various directions and reduced the anisotropy in the assembly.

The new smaller particles created by breakage broadened the particle size distribution [33]. These particles filled the void spaces between the existing particles and formed new contacts along various directions. As a result, the contact orientation anisotropy decreased. It can be argued that any process that broadens the particle size distribution reduces the contact orientation anisotropy. This is in line with the results observed by other researchers [41–44].

As observed in Fig. 10, the anisotropy of the normal contact forces formed vertically during biaxial loading. Moreover, similar to the trend observed for the force chains in Fig. 4, the normal contact forces along the vertical direction increased until reaching peak shear strength and decreased after that. The forces along the horizontal direction remained almost constant during testing. Given the collapse of force chains due to particle breakage in the breakable assembly, it is evident that the normal contact forces decreased vertically compared to that in the non-breakable assembly. This reduced the difference in the values of vertical and horizontal normal contact forces and, subsequently, reduced the anisotropy. In fact, the peanut-shaped histogram became capsular in form.

Figure 11 shows that the shear contact forces increased in the diagonal directions at angles of approximately 45° to the horizontal direction until reaching peak shear strength, and decreased after that. The shape of the histograms reflects the significant difference between the shear forces along the 45° angles and other directions. In fact, the main direction of anisotropy of the shear forces formed along the 45° angles. The nearly fixed shape of the histograms to the end of the testing indicates a slight variation in the anisotropy of the shear forces during the test. Comparison of the non-breakable and

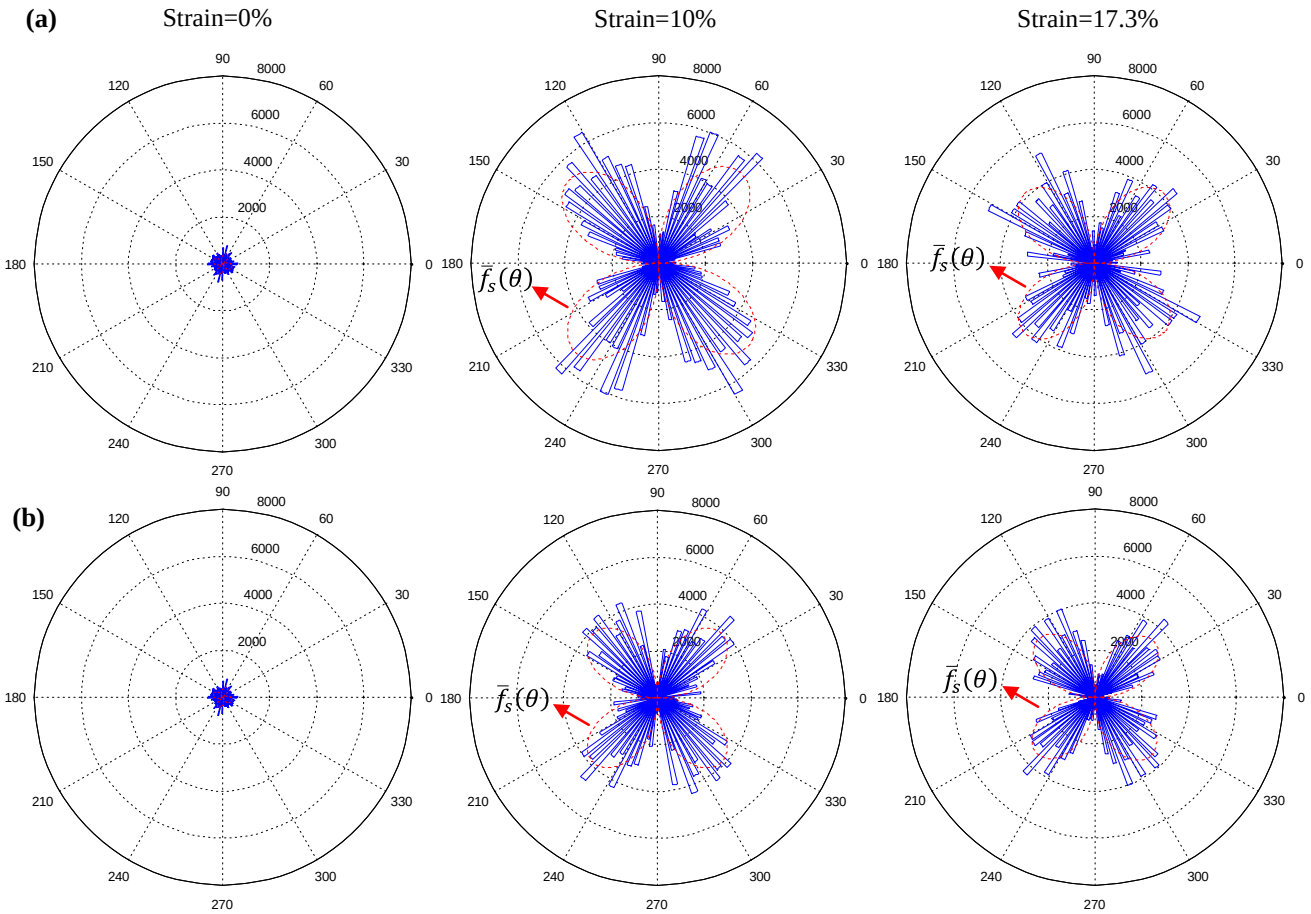

Fig. 11 Histogram of shear contact forces at three strain levels during biaxial testing under a confining pressure of 2 MPa for: **a** non-breakable assembly; **b** breakable assembly

breakable assemblies shows that the shear contact forces decreased mainly along the directions of the anisotropy due to particle breakage. In fact, the difference in the shear forces along the direction of the anisotropy and other directions decreased, causing a decrease in the anisotropy in comparison with the non-breakable assembly. It can be said that strong shear forces which mostly formed along 45° angles were removed due to particle breakage and smaller shear forces were created between the new particles. As a result, a more uniform distribution of contact forces was created and the anisotropy of the shear forces decreased.

Figure 12 shows the variation in the anisotropy of contact orientation, normal and shear contact forces and the total anisotropy during biaxial testing at a confining pressure of 2 MPa. As observed, the anisotropy of contact orientation steadily increased during biaxial testing. However, a number of vertical contacts were lost after peak shear strength due to the collapse of the force chains, causing a decrease in the growth rate of the anisotropy a. A similar trend was observed for the anisotropy in the breakable assembly, but the magnitude of the anisotropy decreased compared to that in the non-breakable assembly. As observed in Fig. 9, new contacts formed in various directions as new particles were created in the breakable assembly. This increased the number of contacts in all directions, resulting a decrease in the anisotropy a of the breakable assembly.

In both the non-breakable and breakable assemblies, the anisotropy of the normal contact forces increased during testing to a peak value, but decreased after reaching peak shear strength. As noted in Sect. 4.1, the normal contact forces along the vertical direction increased as the shear loading increased, while the horizontal contact forces remained almost constant. Therefore, a_n, which is proportional to the difference in the average vertical and horizontal normal contact forces, increased as loading increased. The anisotropy decreased after peak shear strength because of the failure of strong force chains at high stress levels. Also, as mentioned, a number of force chains collapsed because of particle breakage. Hence, the normal contact forces along the vertical direction decreased, leading to a decrease in the anisotropy of the breakable assembly compared to that of the non-breakable assembly.

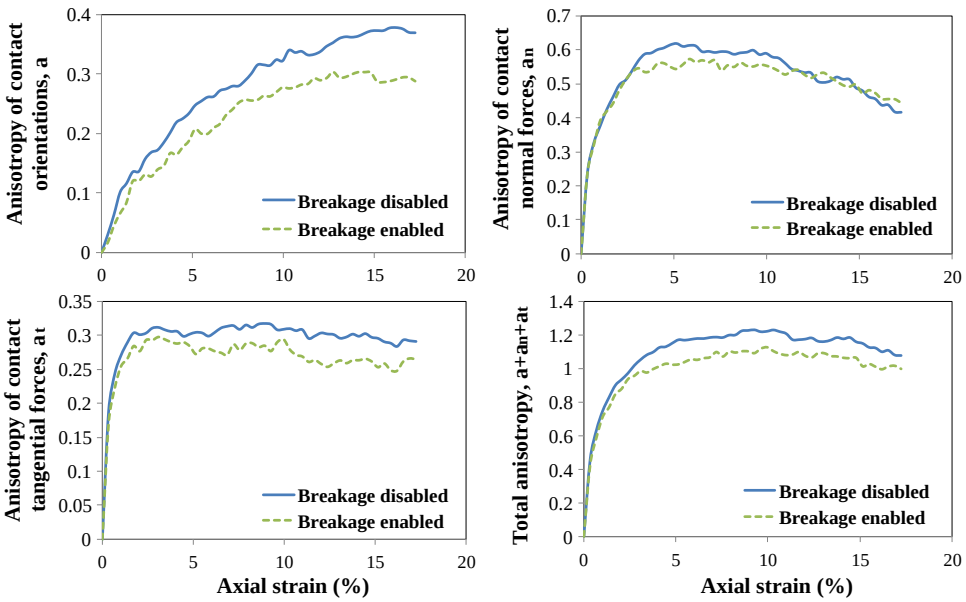

Fig. 12 Variation in anisotropy of contact orientation, normal and shear contact forces and total anisotropy during biaxial testing at a confining pressure of 2 MPa

The anisotropy of shear contact force increased rapidly in the initial stages of loading and remained almost constant during biaxial loading. Figure 11 shows that the difference between the shear forces along the 45° angles and other directions remained almost constant during the test. The anisotropy of the breakable assembly was lower than that of the non-breakable assembly. The new particles created by breakage could rotate more freely between the particles due to their smaller sizes. As a result, the friction between particles and the shear contact forces decreased, leading to a reduction in the anisotropy of the breakable assembly.

As seen in Fig. 12, for both the non-breakable and breakable assemblies, the total anisotropy $a + a_n + a_t$ increased until reaching peak shear strength and then decreased to a residual value at the end of the test. Rothenburg et al. [45] and Rothenburg and Bathurst [46, 47] stated that the macroscopic shear strength of a particle assembly depends on its ability to develop anisotropies. The trend observed for the total anisotropy was similar to that for the macroscopic shear strength which was reported in several laboratory and numerical studies [1, 8, 25–30, 33]. Also, the total anisotropy of the breakable assembly decreased compared to that of the non-breakable assembly. The reduction in the anisotropy due to particle breakage caused a decrease in the macroscopic shear strength of the assembly [33].

In order to more accurately investigate the relationship between anisotropies and macroscopic behavior, the equation proposed by Rothenburg and Bathurst [46, 47] was utilized:

$$\sin\varphi = \frac{\frac{1}{2}\left(a + a_n + a_t\right)}{1 + \frac{aa_n}{2}} \tag{10}$$

where φ is the internal friction angle of the assembly. Because of the small values of $\frac{aa_n}{2}$, Rothenburg and Bathurst [46, 47] introduced a simplified equation by ignoring this term:

$$\sin\varphi = \frac{1}{2}\left(a + a_n + a_t\right) \tag{11}$$

The $\sin\varphi$ calculated using the anisotropy coefficients and Eqs. (10) and (11) was compared with that obtained from macroscopic observation using to the following equation:

$$\sin\varphi = \frac{\sigma_1 - \sigma_2}{\sigma_1 + \sigma_2} \tag{12}$$

where σ_1 and σ_2 are the principal stresses of the particle assembly and along the vertical and horizontal directions in biaxial loading, respectively. σ_2 is constant during the test and equals the confining pressure. The stresses in Eq. (12) were calculated using the common equation for the mean stress tensor of an assembly consisting of discrete particles [48] as:

$$\sigma_{ij} = \frac{1}{A}\sum_{C\in A} f_i^C l_j^C \quad i,j = 1,2 \tag{13}$$

where A is the area of the assembly, f_i^C is the contact force between particles and l_j^C is the contact vector.

Figure 13 compares the $\sin\varphi$ obtained from microscopic and macroscopic results for the non-breakable and breakable assemblies. As seen, the variation in friction angles resulting from Eqs. (10) and (11) has a trend similar to that of the friction angle obtained from macroscopic observations. The friction angle calculated using Eq. (10) shows good agreement with that of the macroscopic results, but the simplified

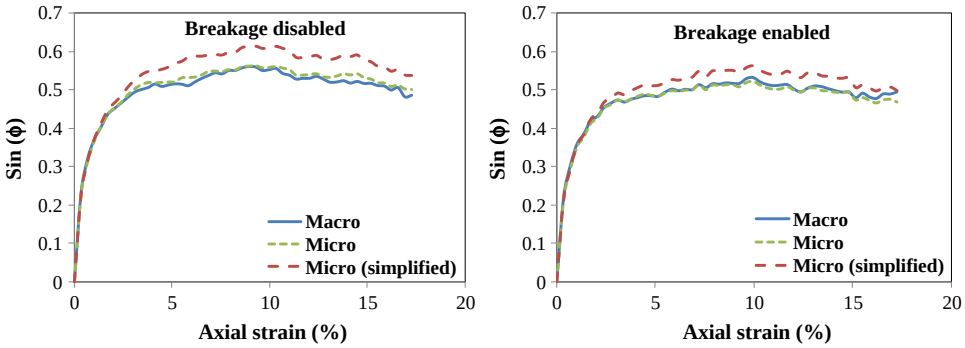

Fig. 13 Relationship between stress and fabric at a confining pressure of 2 MPa for non-breakable and breakable assemblies

Eq. (11) slightly overestimates the friction angles. It can be concluded that the anisotropies of a particle assembly have a direct effect on its macroscopic mechanical behavior.

4.3 Effect of confining pressure

Figure 14 shows the contour of particles displacement at the end of the biaxial test under different confining pressures for the non-breakable and breakable assemblies. Evidently, as confining pressure increased, the lateral displacement of the particle assembly decreased due to increased lateral confinement. It was also observed that the percentage of particle breakage increased as the confining pressure increased and that new particles filled the voids in the assembly. The percentage of particle breakage was considerable at higher confining pressures and a significant portion of the voids were filled with new particles. This decreased the maximum displacement of the particle assembly compared to that of the non-breakable assembly. The decreased displacements caused a decrease in the dilative behavior of the breakable assemblies at higher confining pressures [33].

Figure 15 shows the normal contact force chains under different confining pressures at peak shear strength for the breakable and non-breakable assemblies. As expected, moderate and strong contact forces increased as the level of stress increased. Moreover, in the breakable assembly, the magnitude of the contact forces decreased and a more uniform distribution of contact forces was observed. A slight reduction in the contact forces was observed at lower confining pressures due to the low percentage of particle breakage, but the reduction in contact forces, especially strong contact forces, was evident at higher confining pressures.

A trend similar to that of the force chains was observed for the distribution of vertical particle stresses, as shown in Fig. 16. The number of particles with high stresses decreased as the confining pressure increased. Because particle breakage increased at higher confining pressures, a number of stress concentrations were removed, decreasing the number of particles with high stresses in the breakable assemblies.

The number of particles at different levels of displacement and stress and the number of forces at different levels were measured in Figs. 14, 15 and 16, as shown in Table 3, for a quantitative comparison. The obtained results are in line with the observations noted before. As seen in Table 3, because of the lateral confinement caused by high confining pressures, the number of particles having large displacements decreased as the confining pressure increased. Also, the number of strong forces and particles under high stresses increased at higher confining pressures. It was observed that the number of particles experiencing large displacements, strong contact forces and high stresses in the breakable assembly decreased significantly compared to that in the non-breakable assembly at higher confining pressures. In fact, the effects of particle breakage intensified at higher confining pressures.

The void ratio of the particle assembly has been computed at the end of each biaxial test to quantitatively compare the void spaces of the non-breakable and breakable assemblies. Table 4 shows the final void ratio of the non-breakable and breakable assemblies at different confining pressures. The obtained data shows that particle breakage reduced the void ratio of the assembly at each confining pressure. The displacements measured in Figs. 3 and 14, as presented in Tables 2 and 3, showed that the particle breakage caused a decrease in the overall displacement of the assembly. Therefore, it can be concluded that new particles created by breakage filled the voids in the assembly. Reduction in voids decreased the final displacement of the particle assembly.

Figure 17 shows the polar distribution of contact orientation under different confining pressures at peak shear strength for the non-breakable and breakable assemblies. It can be observed that the number of contacts increased slightly as the confining pressure increased. Because the vertical strain of the assembly was almost the same at different confining pressures, the number of contacts did not significantly increase along the vertical direction. The number of contacts increased along the horizontal direction, because the lateral confinement of high stress levels reduced the lateral expansion of the assembly, as can be observed in Fig. 14. This produced a more uniform distribution of number of contacts along different directions at

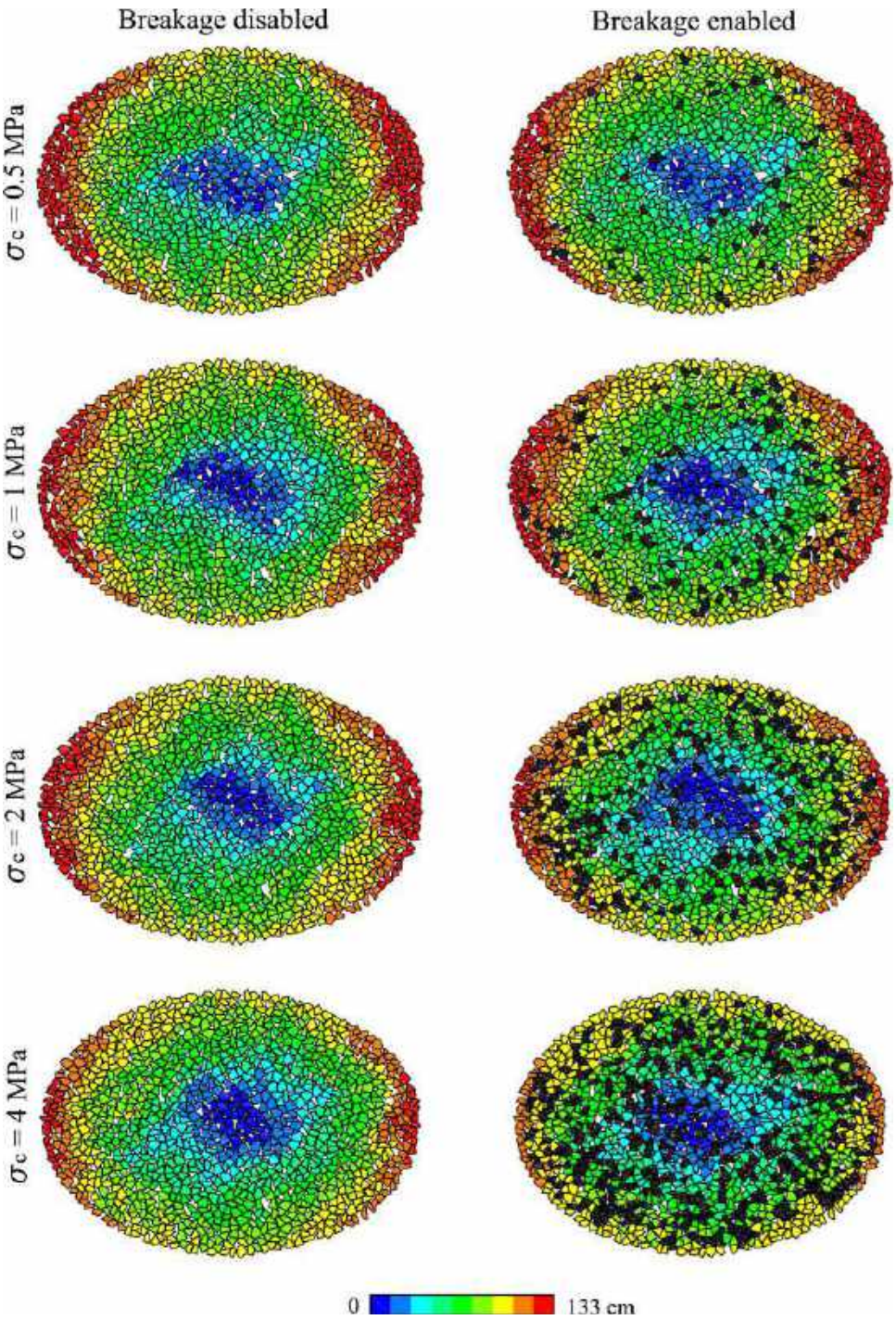

Fig. 14 Contour of particles displacement at the end of biaxial test under different confining pressures for non-breakable and breakable assemblies

high confining pressures and, consequently, reduced the anisotropy. It also can be observed that a significant number of new contacts formed by the new particles created by breakage at high confining pressures and the number of contacts increased in various directions. It can be stated that particle breakage, especially at high confining pressures, resulted in a more isotropic assembly and reduced the anisotropy of contact orientation.

Figures 18 and 19 show the polar distribution of the normal and shear contact forces, respectively, under different confining pressures at peak shear strength for the non-breakable and breakable assemblies. Figure 18 reveals that the contact forces increased mostly in the vertical direction as the confining pressure increased. Figure 19 reveals that the shear contact forces increased mainly at 45° angles, which are the direction of anisotropy. Because of the lateral

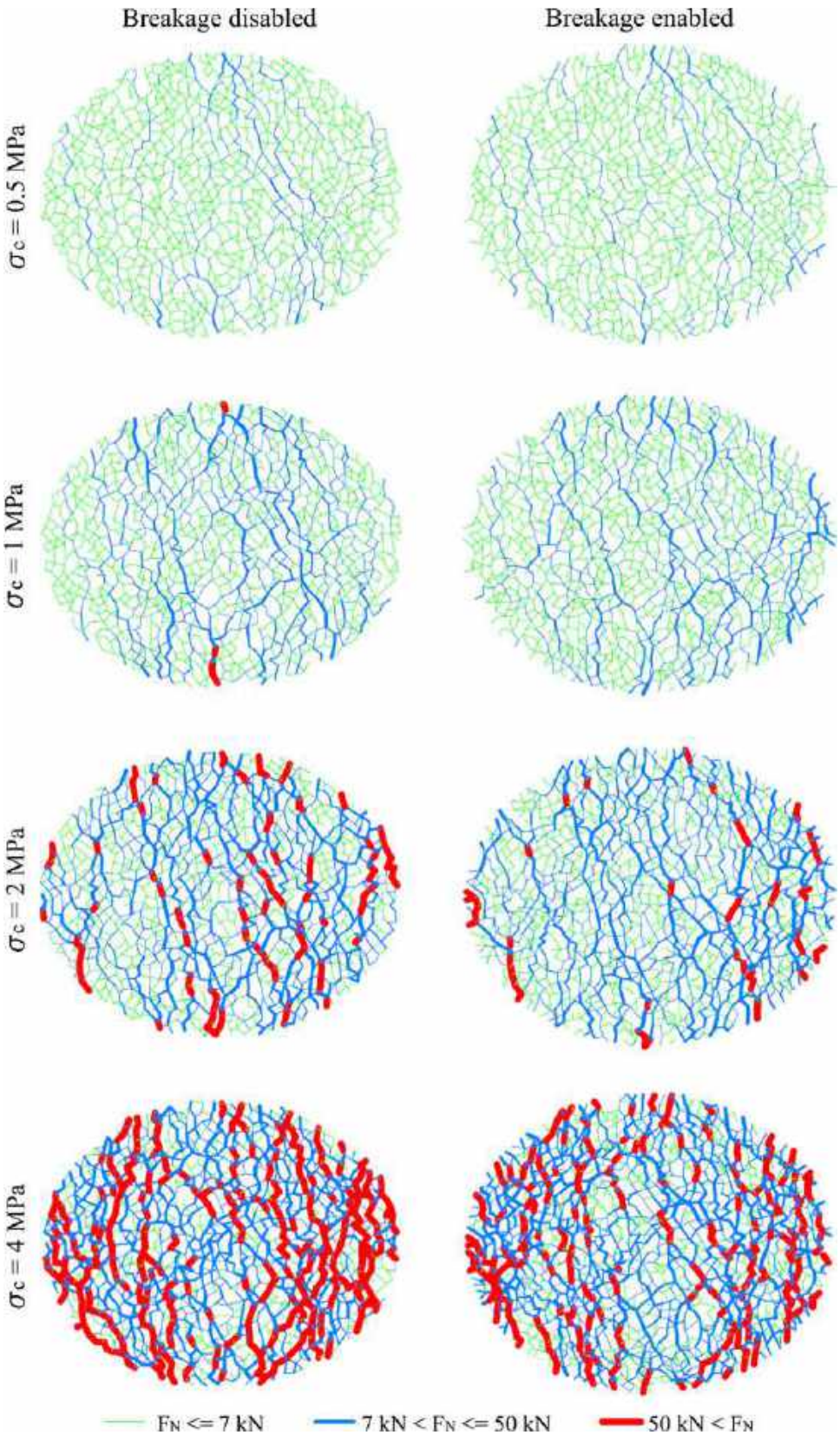

Fig. 15 Normal contact force chains at peak shear strength under different confining pressures for non-breakable and breakable assemblies

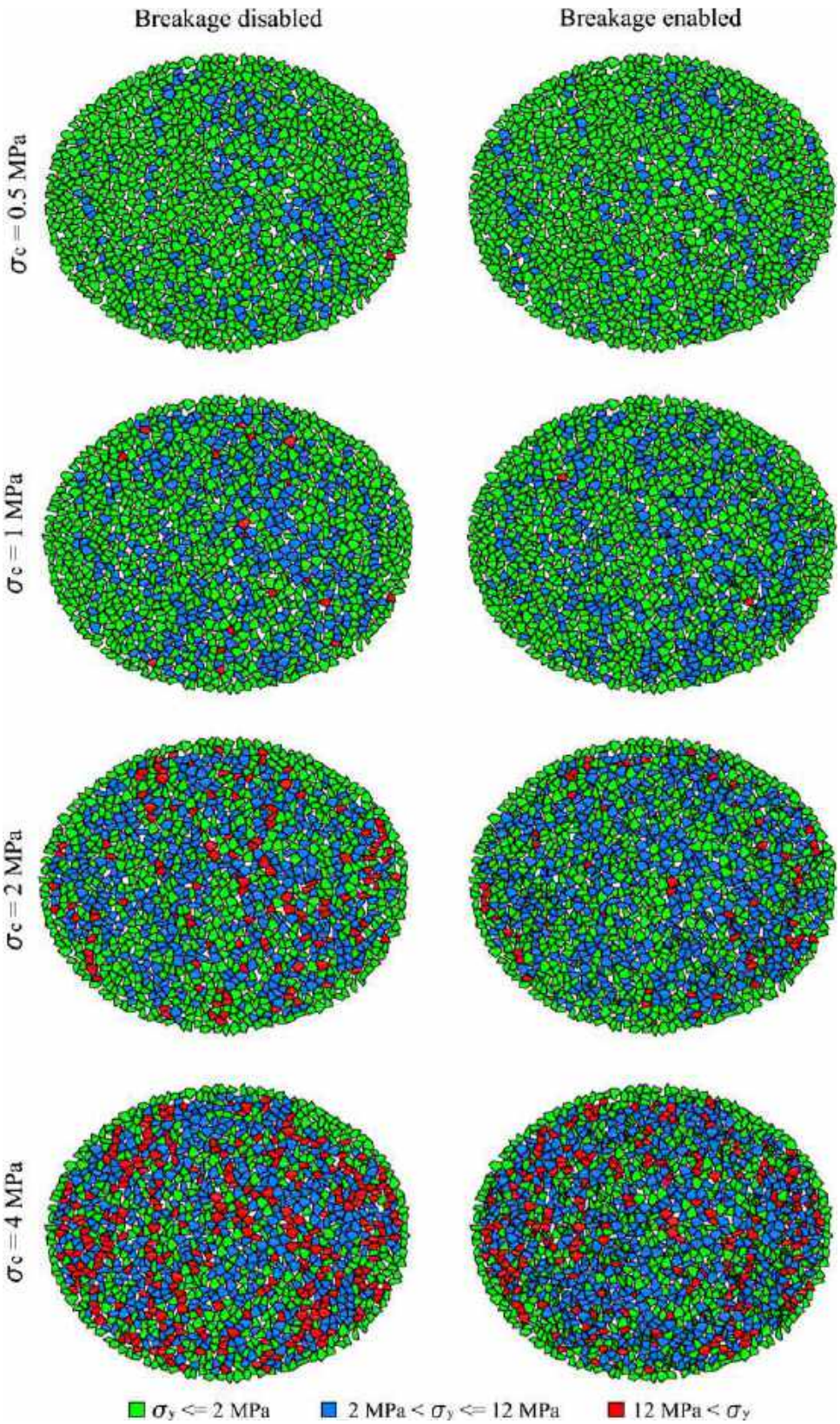

Fig. 16 Distribution of vertical particle stresses at peak shear strength under different confining pressures for non-breakable and breakable assemblies

Table 3 Number of particles having large displacements at the end of test and number of forces and stresses at peak shear strength under different confining pressures

Confining pressure (MPa)	Non-breakable assembly				Breakable assembly			
	0.5	1	2	4	0.5	1	2	4
Number of large displacements (> 118 cm) at the end of test	120	101	86	35	112	87	41	1
Number of weak forces	1454	1029	661	386	1527	1231	938	686
Number of moderate forces	390	853	1165	1224	371	857	1344	1695
Number of strong forces	0	9	121	418	0	0	56	315
Number of low vertical stresses	988	767	586	426	1051	899	824	765
Number of medium vertical stresses	204	408	476	469	183	387	527	580
Number of high vertical stresses	2	19	132	299	0	2	60	217

Table 4 Void ratio of particle assembly at the end of biaxial test for non-breakable and breakable assemblies under different confining pressures

Confining pressure (MPa)	0.5	1	2	4
Void ratio of non-breakable assembly	0.360	0.351	0.336	0.314
Void ratio of breakable assembly	0.358	0.339	0.316	0.288

confinement caused by high confining pressures, bulking of the force chains, which formed mainly in the vertical direction, occurred at higher stress levels. As a result, the magnitude of the normal contact forces increased. At high confining pressures, friction between particles was higher, which increased the magnitude of the shear contact forces. Comparison of the non-breakable and breakable assemblies shows a significant decrease in normal and shear contact forces due to the increase in breakage at higher confining pressures.

Figure 20 shows the variation in the anisotropies during biaxial testing at different confining pressures for the non-breakable and breakable assemblies. As was observed in Fig. 17, the anisotropy of the contact orientation decreased as the confining pressure increased. An increase in confining pressure increased the percentage of particle breakage and new contacts in various directions. Therefore, a greater decrease in anisotropy was observed for the breakable assembly at higher confining pressures compared to that of the non-breakable assembly.

As seen in Fig. 20, the anisotropy of normal contact forces remained almost constant at different confining pressures in the non-breakable assembly, but showed a small decrease in the breakable assembly with an increase in the confining pressure. The collapse of force chains caused by particle breakage reduced the vertical normal contact forces at higher confining pressures and, consequently, the anisotropy of normal forces.

As for normal forces, the anisotropy of the shear contact forces showed nearly constant values at different confining pressures in the non-breakable assembly. An almost similar trend could be observed for the breakable assembly. In fact, the anisotropy of the breakable assembly decreased almost the same at different confining pressures compared to that of the non-breakable assembly.

The effect of confining pressure on the total anisotropy, $a + a_n + a_t$, was compared for the non-breakable and breakable assemblies. Figure 20 shows that the total anisotropy decreased slightly in the non-breakable assembly as the confining pressure increased. However, in the breakable assembly, a significant decrease in the total anisotropy was observed with an increase in the confining pressure. It could be concluded that the particle breakage was the main factor for the reduction in the total anisotropy at higher confining pressures.

The relationship between the anisotropy coefficients and macroscopic behavior was investigated at different confining pressures using Eq. (10), which showed better correlation with macroscopic behavior, as was observed in Fig. 13. In Fig. 21, the $\sin\varphi$ derived from the anisotropy coefficients was compared with that calculated from the macroscopic results for the non-breakable and breakable assemblies. Figure 22 shows the peak friction angle φ_{peak} obtained from the anisotropy coefficients and the macroscopic results. These figures show that there is a good agreement between the friction angles calculated from the anisotropy coefficients and the macroscopic results. It was observed that the results of Eq. (10) provide a more accurate estimation for the non-breakable assemblies. Overall, the results show a direct relationship between microscopic and macroscopic behavior. It can be concluded that the development of anisotropies is the main cause of the development of shear strength in granular materials and the particle breakage reduces the shear strength of the assembly by reducing the anisotropies.

Figure 21 shows that particle breakage reduced the shear strength, especially at higher confining pressures, but the residual shear strength was nearly the same for the non-breakable and breakable assemblies. However, it can be seen that the residual shear strength of the breakable assembly was slightly lower than that of the breakable assembly at a confining pressure of 4 MPa. Overall, it can be claimed that

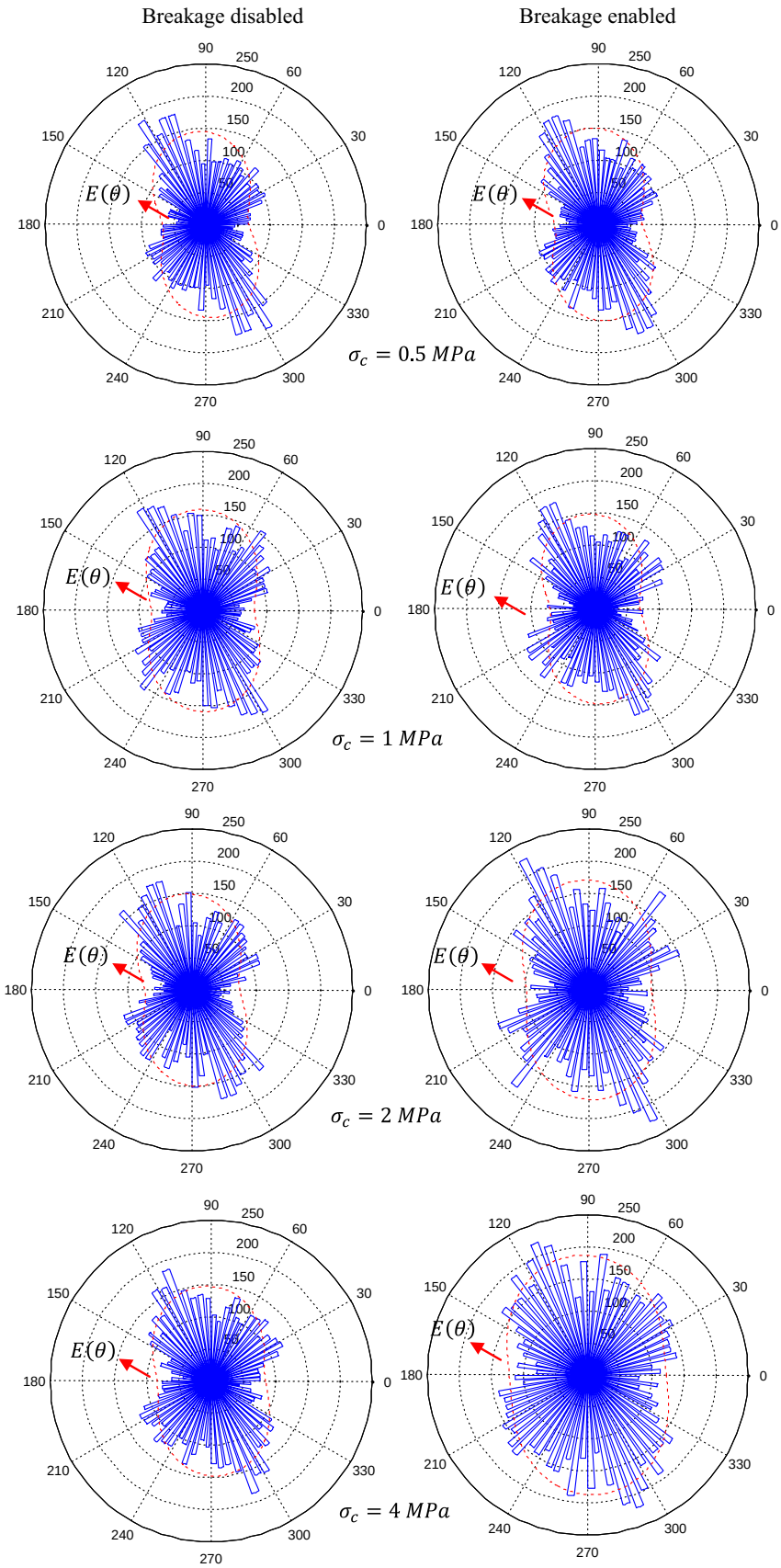

Fig. 17 Histogram of contact orientation at peak shear strength under different confining pressures

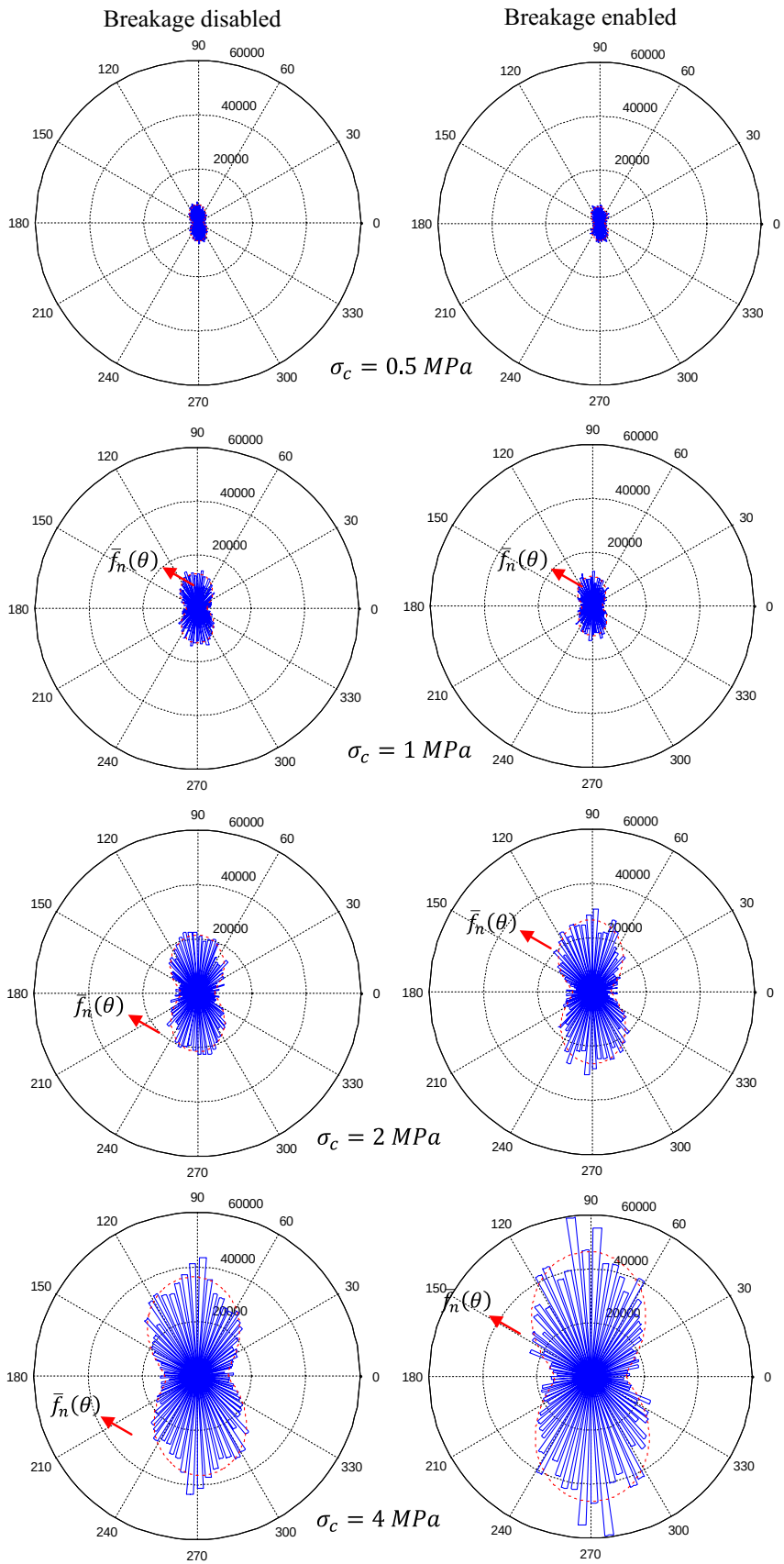

Fig. 18 Histogram of normal contact forces at peak shear strength under different confining pressures

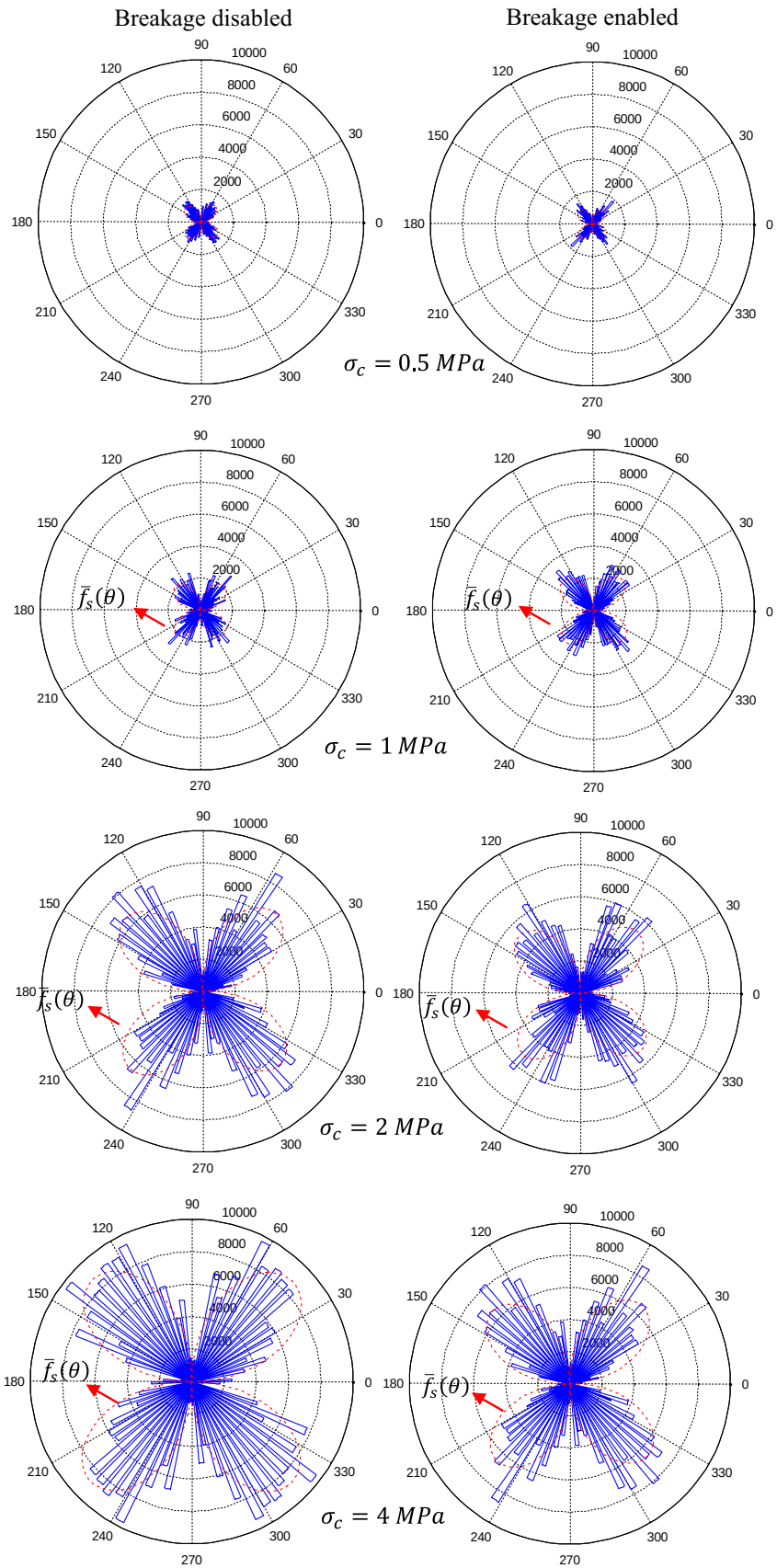

Fig. 19 Histogram of shear contact forces at peak shear strength under different confining pressures

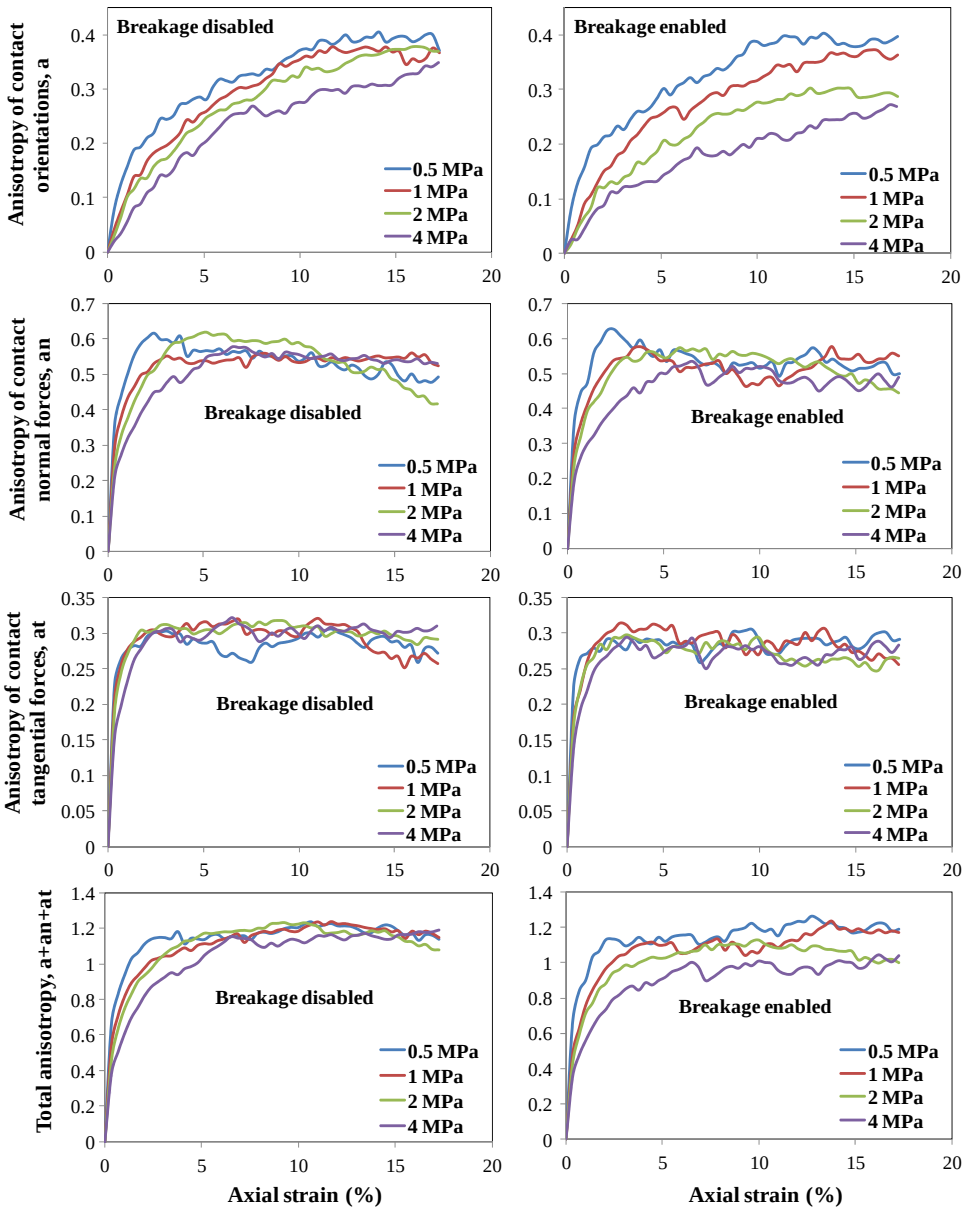

Fig. 20 Variation in anisotropy of contact orientation, normal and shear contact forces and total anisotropy at different confining pressures for non-breakable and breakable assemblies

the residual shear strength is almost independent of particle breakage. In line with these observations, other studies [42, 43, 49] have reported that residual shear strength is independent of the particle size distribution.

5 Summary and conclusions

In the present study, particle breakage was simulated in two-dimensional angular rockfill materials under biaxial compression loading using a new combined DEM and XFEM approach. Simulation of the biaxial compression test on the particle assembly was performed by DEM. Breakage analysis was carried out separately on each particle using XFEM at small time intervals during loading. In the breakage analysis, the particle was meshed and analyzed for crack initiation or crack propagation under contact loads from adjacent particles. Progressive strength reduction of the particles during loading was modeled because each breakage analysis was performed based on the crack propagation in the previous steps.

Qualitative agreement between the results of the numerical simulations and experimental data was observed. Biaxial test simulations on both non-breakable and breakable particle assemblies were performed at different confining pressures and the micromechanical behavior of the particle assemblies was studied. The main findings were:

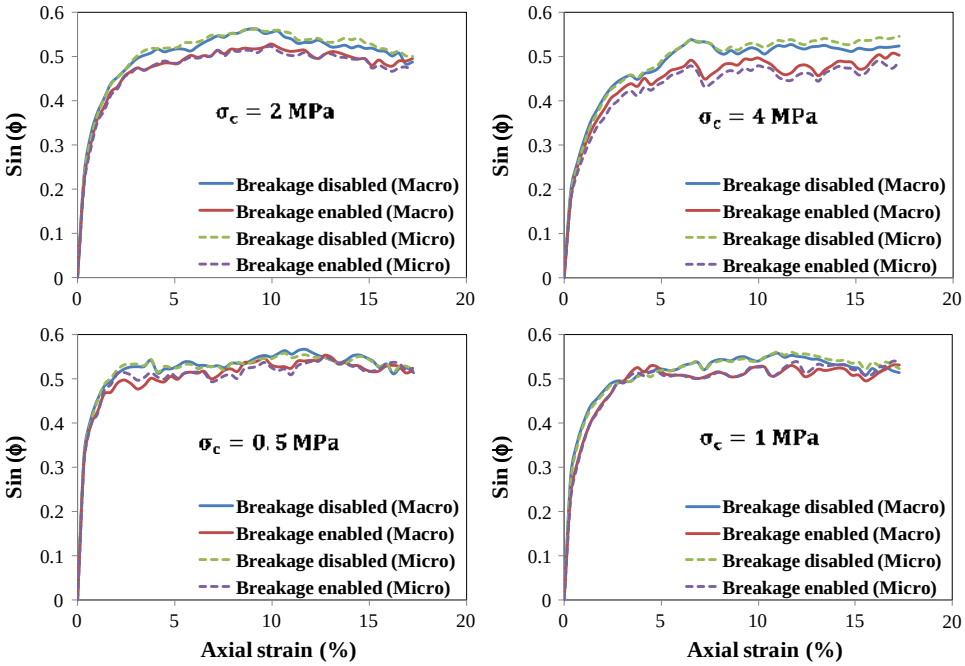

Fig. 21 Relationship between stress and fabric at different confining pressures for non-breakable and breakable assemblies

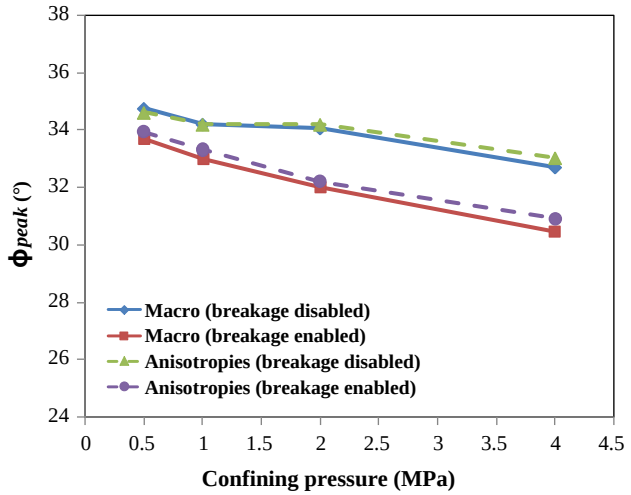

Fig. 22 Peak friction angles obtained from microscopic and macroscopic results at different confining pressures for non-breakable and breakable assemblies

- New particles created by breakage filled the voids in the assembly. Reduction in voids decreased the final displacement of the particle assembly.
- Contact force chains failed due to breakage of their constituent particles. As a result, the magnitude of the contact forces and the number of particles with high stresses decreased. Overall, particle breakage caused a more uniform distribution of contact forces and particle stresses in the assembly.
- Anisotropies caused the development of macroscopic shear strength in the assembly. Particle breakage reduced the shear strength of the assembly by reducing the anisotropies.
- The percentage of particle breakage increased as the confining pressure increased and led to a further decrease in the final displacement of the assembly, contact forces and particle stresses.
- The anisotropy of contact orientation decreased at higher stress levels, but the anisotropy of normal and shear contact forces remained almost constant in the non-breakable assembly. In fact, particle breakage was the main factor for the reduction in the total anisotropy at higher confining pressures. Reduction of in the anisotropy led to a decrease in the peak friction angle of the assembly.

Compliance with ethical standards

Conflict of interest The authors declare that they have no conflict of interest.

References

1. Marsal, R.J.: Large-scale testing of rockfill materials. J. Soil Mech. Found. Div. **93**(2), 27–43 (1967)
2. Marachi, N.D., Chan, C.K., Seed, H.B.: Evaluation of properties of rockfill materials. J. Soil Mech. Found. Div. **97**(SM1), 95–114 (1971)
3. Charles, J.A., Watts, K.S.: The influence of confining pressure on the shear strength of compacted rockfill. Geotechnique **30**(4), 353–367 (1980)

4. Hardin, B.O.: Crushing of soil particles. J. Geotech. Eng. **111**(10), 1177–1192 (1985)
5. Lade, P.V., Yamamuro, J.A.: Undrained sand behavior in axisymmetric tests at high pressures. J. Geotech. Eng. **122**(2), 120–129 (1996)
6. Yamamuro, J.A., Lade, P.V.: Drained sand behavior in axisymmetric tests at high pressures. J. Geotech. Eng. **122**(2), 109–119 (1996)
7. Lade, P.V., Yamamuro, J.A., Bopp, P.A.: Significance of particle crushing in granular materials. J. Geotech. Eng. **122**(4), 309–316 (1996)
8. Varadarajan, A., Sharma, K.G., Venkatachalam, K., Gupta, A.K.: Testing and modeling two rockfill materials. J. Geotech. Geoenviron. Eng. **129**(3), 206–218 (2003)
9. Cundall, P.A., Strack, O.D.: A discrete numerical model for granular assemblies. Geotechnique **29**(1), 47–65 (1979)
10. Kun, F., Herrmann, H.J.: A study of fragmentation processes using a discrete element method. Comput. Methods Appl. Mech. Eng. **138**, 3–18 (1996)
11. Potapov, A.V., Campbell, C.S.: Computer simulation of impact-induced particle breakage. Powder Technol. **81**(3), 207–216 (1994)
12. Potapov, A.V., Campbell, C.S.: Parametric dependence of particle breakage mechanisms. Powder Technol. **120**(3), 164–174 (2001)
13. Sheikh, B., Pak, A.: Numerical investigation of the effects of porosity and tortuosity on soil permeability using coupled three-dimensional discrete-element method and lattice Boltzmann method. Phys. Rev. E **91**(5), 053301-1–053301-14 (2015)
14. Sheikh, B., Qiu, T.: Pore-scale simulation and statistical investigation of velocity and drag force distribution of flow through randomly-packed porous media under low and intermediate Reynolds numbers. Comput. Fluids **171**, 15–28 (2018)
15. Cantor, D., Estrada, N., Azéma, E.: Split-cell method for grain fragmentation. Comput. Geotech. **67**, 150–156 (2015)
16. Nguyen, D.H., Azéma, E., Sornay, P., Radjai, F.: Bonded-cell model for particle fracture. Phys. Rev. E **91**(2), 022203 (2015)
17. Nguyen, D.H., Azéma, E., Sornay, P., Radjai, F.: Rheology of granular materials composed of crushable particles. Eur. Phys. J. E **41**(4), 50–60 (2018)
18. Robertson, D., Bolton, M.D.: DEM simulations of crushable grains and soils. Powders Grains **1**, 623–626 (2001)
19. McDowell, G.R., Harireche, O.: Discrete element modelling of soil particle fracture. Geotechnique **52**(2), 131–135 (2002)
20. Cheng, Y.P., Bolton, M.D., Nakata, Y.: Crushing and plastic deformation of soils simulated using DEM. Geotechnique **54**(2), 131–141 (2004)
21. Bolton, M.D., Nakata, Y., Cheng, Y.P.: Micro-and macro-mechanical behaviour of DEM crushable materials. Geotechnique **58**(6), 471–480 (2008)
22. McDowell, G.R., de Bono, J.P.: On the micro mechanics of one-dimensional normal compression. Geotechnique **63**(11), 895–908 (2013)
23. de Bono, J.P., McDowell, G.R.: DEM of triaxial tests on crushable sand. Granul. Matter **16**(4), 551–562 (2014)
24. de Bono, J.P., McDowell, G.R.: Particle breakage criteria in discrete-element modelling. Geotechnique **66**(12), 1014–1027 (2016)
25. Hosseininia, E.S., Mirghasemi, A.A.: Numerical simulation of breakage of two-dimensional polygon-shaped particles using discrete element method. Powder Technol. **166**(2), 100–112 (2006)
26. Hosseininia, E.S., Mirghasemi, A.A.: Effect of particle breakage on the behavior of simulated angular particle assemblies. Particuology **5**(5), 328–336 (2007)
27. Bagherzadeh-Khalkhali, A., Mirghasemi, A.A., Mohammadi, S.: Micromechanics of breakage in sharp-edge particles using combined DEM and FEM. Particuology **6**(5), 347–361 (2008)
28. Bagherzadeh-Khalkhali, A., Mirghasemi, A.A., Mohammadi, S.: Numerical simulation of particle breakage of angular particles using combined DEM and FEM. Powder Technol. **205**(1), 15–29 (2011)
29. Luo, T., Ooi, E.T., Chan, A.H., Fu, S.J.: The combined scaled boundary finite-discrete element method: grain breakage modelling in cohesion-less granular media. Comput. Geotech. **88**, 199–221 (2017)
30. Ma, G., Zhou, W., Chang, X.L.: Modeling the particle breakage of rockfill materials with the cohesive crack model. Comput. Geotech. **61**, 132–143 (2014)
31. Ma, G., Zhou, W., Chang, X.L., Chen, M.X.: A hybrid approach for modeling of breakable granular materials using combined finite-discrete element method. Granul. Matter **18**(1), 7 (2016)
32. Ma, G., Zhou, W., Regueiro, R.A., Wang, Q., Chang, X.: Modeling the fragmentation of rock grains using computed tomography and combined FDEM. Powder Technol. **308**, 388–397 (2017)
33. Raisianzadeh, J., Mirghasemi, A.A., Mohammadi, S.: 2D simulation of breakage of angular particles using combined DEM and XFEM. Powder Technol. **336**, 282–297 (2018)
34. Mirghasemi, A.A., Rothenburg, L., Matyas, E.L.: Numerical simulations of assemblies of two-dimensional polygon-shaped particles and effects of confining pressure on shear strength. Soils Found. **37**(3), 43–52 (1997)
35. Mirghasemi, A.A., Rothenburg, L., Matyas, E.L.: Influence of particle shape on engineering properties of assemblies of two-dimensional polygon-shaped particles. Geotechnique **52**(3), 209–217 (2002)
36. O'Sullivan, C.: Particulate Discrete Element Modelling: A Geomechanics Perspective. Spon Press (an imprint of Taylor & Francis), London (2011)
37. Mohammadi, S.: Extended Finite Element Method: For Fracture Analysis of Structures. Blackwell Publishing, Oxford (2008)
38. Mohammadi, S.: XFEM Fracture Analysis of Composites. Wiley, Hoboken (2012)
39. Hoek, E., Brown, E.T.: Practical estimates of rock mass strength. Int. J. Rock Mech. Min. Sci. **34**(8), 1165–1186 (1997)
40. Lambe, T.W., Whitman, R.V.: Soil Mechanics SI Version. Wiley, New York (2008)
41. Voivret, C., Radjai, F., Delenne, J.Y., El Youssoufi, M.S.: Multiscale force networks in highly polydisperse granular media. Phys. Rev. Lett. **102**(17), 178001 (2007)
42. Voivret, C., Radjai, F., Delenne, J.Y., El Youssoufi, M.S.: Space-filling properties of polydisperse granular media. Phys. Rev. E **76**(2), 021301 (2009)
43. Azéma, E., Linero, S., Estrada, N., Lizcano, A.: Shear strength and microstructure of polydisperse packings: the effect of size span and shape of particle size distribution. Phys. Rev. E **96**(2), 022902 (2017)
44. Estrada, N., Oquendo, W.F.: Microstructure as a function of the grain size distribution for packings of frictionless disks: effects of the size span and the shape of the distribution. Phys. Rev. E **96**(4), 042907 (2017)
45. Rothenburg, L., Bathurst, R.J., Dusseault, M.B.: Micromechanical ideas in constitutive modelling of granular materials. In: Biarez, J., Gourves, R. (eds.) Powders and Grains, pp. 355–363. Balkema, Rotterdam (1989)
46. Rothenburg, L., Bathurst, R.J.: Analytical study of induced anisotropy in idealized granular materials. Geotechnique **39**(4), 601–614 (1989)

47. Rothenburg, L., Bathurst, R.J.: Micromechanical features of granular assemblies with planar elliptical particles. Geotechnique **42**(1), 79–95 (1992)
48. Rothenburg, L.: Micromechanics of idealized granular systems. Doctoral Dissertation, Department of Civil Engineering, Carlton University, Ottawa, Canada (1980)
49. Estrada, N.: Effects of grain size distribution on the packing fraction and shear strength of frictionless disk packings. Phys. Rev. E **94**(6), 062903 (2016)